

# Hessian Analysis Enables Prediction of Cytoquake Occurrence

Carlos Floyd

*Biophysics Program, University of Maryland, College Park, MD 20742 USA*

Herbert Levine

*Department of Bioengineering and  
Department of Physics, Northeastern University, Boston, MA 02115 USA*

Christopher Jarzynski\*

*Department of Chemistry and Biochemistry,  
Institute for Physical Science and Technology, and  
Department of Physics, University of Maryland, College Park, MD 20742 USA*

Garegin A. Papoian†

*Department of Chemistry and Biochemistry and  
Institute for Physical Science and Technology,  
University of Maryland, College Park, MD 20742 USA  
(Dated: December 22, 2024)*

Eukaryotic cells are mechanically supported by a polymer network called the cytoskeleton, which continually consumes chemical energy so that it may dynamically remodel its structure. Recent experiments revealed that this remodeling process occasionally happens through unusually large, step-like events reminiscent of earthquakes. These rare events, termed “cytoquakes,” may reflect optimized information processing by cytoskeletal networks, and are hence of significant biological interest. The physics underlying cytoquakes are poorly understood, however, hindering investigation of their possible biological roles. We address this gap by using agent-based simulations of cytoskeletal self-organization to show that cytoquakes’ origins lie in the inherent driven, dissipative dynamics of active cytoskeletal networks. In a near-critical stochastic process, strain energy accumulates before being released in large, global restructuring events. By forecasting cytoquakes using a machine learning model, we furthermore show that mechanical instability precedes cytoquakes, which then induce a spatial homogenization of tension sustained by the network.

## I. INTRODUCTION

The actin-based cytoskeleton is an active biopolymer network that plays a central role in cellular physiology, providing the cell with a means to control its shape and produce mechanical forces during processes such as migration and cytokinesis [1, 2]. These cellular-level forces arise from the collective non-equilibrium activity of molecular motors interacting with the actin filament scaffold, enabling dynamic cytoskeletal remodeling [3–5]. Recent experimental efforts have uncovered a remarkable phenomenon exhibited by cytoskeletal networks *in vivo*: these networks undergo large, sudden structural rearrangements significantly more frequently than predicted by a Gaussian distribution [6, 7]. In previous work we have reported the first *in silico* observations of this phenomenon, appearing as heavy tails in the distributions of mechanical energy released by cytoskeletal networks [8]. These findings suggest that

avalanche-like processes may play a fundamental role in cytoskeletal dynamics.

Heavy-tailed distributions of event sizes are well-known in seismology, where the Gutenberg-Richter law describes the power-law relationship between the energy released by an earthquake and such an earthquake’s frequency [9, 10]. Due to this analogy the term “cytoquake,” which we adopt here, has been coined by experimenters to describe large cytoskeletal remodeling events [6].

Despite being experimentally well-documented, cytoquakes have so far remained an underappreciated biophysical phenomenon, for perhaps two reasons. First, cytoquakes and their origins have not been concretely explained in terms of the mechanochemical properties of cytoskeletal networks. This is partly due to limited experimental access to important dynamic quantities of these networks, such as the mechanical strain energy and cross-linker and motor binding topologies. As a result, current explanations are speculative and rely on qualitative comparisons to systems amenable to computational study which similarly exhibit non-exponential relaxation, such as jammed granular packings and spin glasses [6, 7, 11, 12]. A concrete

\* cjarzyns@umd.edu

† gpapoian@umd.edu

physical theory of cytoquakes would have the practical benefit of enabling improvements to traction-based experimental methodologies, which have suffered from an incomplete understanding of mechanical dissipation in cytoskeletal networks [13]. Second, little emphasis has been given to the possible biological roles played by cytoquakes. We propose one such role, that in order to be highly sensitive to physiological cues arriving via various cell signaling pathways, the cytoskeleton may operate near the “edge of chaos” where it can respond to such cues in a global yet coherent way [14]. Dynamic instability is already an acknowledged feature of certain cytoskeletal components such as microtubules and filopodia [15, 16]. Perhaps a similar design principle applies to larger cytoskeletal structures as well, to allow such structures to undergo fast remodeling. We can draw an analogy to familiar systems like the Ising model which have large susceptibilities to applied fields when near criticality [17]. However, to investigate such possible biological roles we first need a more detailed and evidence-based account of cytoquake physics, which is the subject of this paper.

Here, we use an agent-based simulation platform called MEDYAN (Mechanochemical Dynamics of Active Networks) to simulate self-organizing cytoskeletal networks at high spatio-temporal resolution, allowing us to develop a physical theory of cytoquakes. We focus on a minimal, sufficient model system and center our study on the system’s mechanical energy, finding that the process of energy accumulation and release is a self-affine random walk in a rugged landscape. A finite-size scaling analysis reveals that for the physiological conditions tested here, cytoskeletal networks exhibit dynamics close to, but not at, a state of self-organized criticality (SOC), resulting in the non-Gaussian releases of energy we identify as cytoquakes. These cytoquake events are observed to correspond to unusually large, global filament displacements as well as a spatial homogenization of tension sustained by the network. We augment our study using Hessian analysis to obtain the network’s vibrational normal modes, which has not previously been done for cytoskeletal networks. We characterize the normal mode spectrum across various experimental conditions and demonstrate that cytoquakes involve enhanced displacement along the network’s soft modes. Finally, we implement a machine learning model which reliably forecasts cytoquake occurrence given the normal mode spectrum, showing that avalanche-like relaxation events are preceded by mechanically unstable network configurations.

These results indicate that cytoquakes are an emergent mechanochemical phenomenon resulting

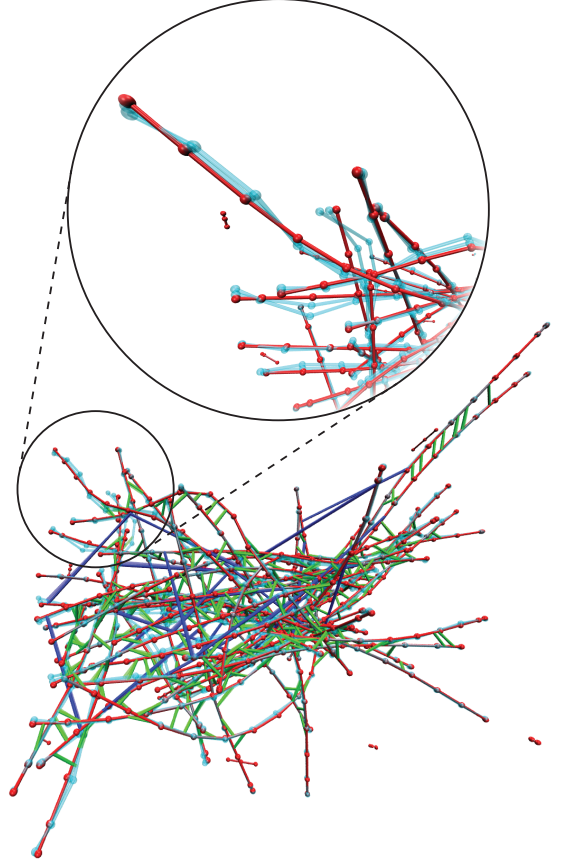


FIG. 1. A snapshot from a MEDYAN trajectory of an actomyosin network in a  $1 \mu\text{m}^3$  box for the condition  $C_{3,3}$ . Actin filaments are shown in red,  $\alpha$ -actinin is shown in green, and myosin motors are shown in blue. Beads representing the joined points (i.e. hinges) of thin cylinders (here  $54 \text{ nm}$  long) are visualized as red spheres. The cyan filaments represent motion of the network corresponding to a soft, delocalized vibrational mode determined from Hessian analysis, as described in the main text. In the inset we zoom in on part of the network and exclude associated proteins to show greater detail of this vibrational motion.

from the cytoskeleton’s inherent driven, dissipative dynamics, similar to SOC earth systems. In a subcritical process, mechanical energy gradually accumulates in the system and is released in large restructuring events which are triggered by unstable network configurations and which result in homogenization of the network’s tension. These new insights are congruous with experimental results and can provide an interpretive framework for future studies of cytoquakes and their biological roles.

## II. RESULTS

### A. Energy fluctuations are heavy-tailed and self-affine

To computationally study cytoskeletal networks at high resolution, we used the simulation platform MEDYAN [8, 18–21]. MEDYAN simulations combine stochastic chemical dynamics with a mechanical representation of filaments and associated proteins (see the Supplementary Material for a detailed description of the MEDYAN model). We simulated cytoskeletal networks across a range of cross-linker and myosin motor concentrations with a fixed concentration of actin filaments and subunits (see Methods). Simulations proceed iteratively in a sequence of four steps: 1) stochastic chemical simulation for a time  $\delta t$  (here 0.05 s), 2) computation of the resulting new forces, 3) quasi-equilibration via minimization of the mechanical energy, and 4) updating of force-sensitive reaction rates. Recent extensions to the MEDYAN platform allow calculation of the change in the system's Gibbs free energy during each of these steps [8, 22]. This extension was originally applied to study the thermodynamic efficiency of the myosin motors in converting chemical free energy to mechanical energy under various conditions of cross-linker and myosin motor concentration. We employ this methodology here and focus on the statistics of the system's mechanical energy  $U$  as it self-organizes.

We first characterize the observed occurrence of cytoquakes in these simulations. The simulations begin with short seed filaments that quickly polymerize (tens of seconds) to their equilibrium lengths. Following this, the slower process (hundreds of seconds) of dominantly myosin-driven self-organization occurs which for most conditions results in geometric contraction to a percolated network (see SI Movie 1) [23, 24]. The mechanical energy  $U(t)$  fluctuates near a quasi-steady state (QSS) value, which we analyze as a stochastic process.

In Figure 2.A we display the trajectory of  $U(t)$  for condition  $C_{3,3}$  ( $[\alpha] = 2.82 \mu M$ ,  $[M] = 0.04 \mu M$ ). We tracked the net changes of the mechanical energy  $\Delta U(t) = U(t + \delta t) - U(t)$  (labeled as  $\Delta G_{\text{mech}}$  in Ref. 8) resulting from each complete cycle of simulation steps 1) - 4). For the purpose of analyzing the asymmetric heavy tails in the distribution of  $\Delta U$ , we treat the negative increments  $\Delta U_-$  (energy release) and positive increments  $\Delta U_+$  (energy accumulation) as samples from separate distributions with semi-infinite domains. The complementary cumulative distribution functions (CCDFs, i.e. the probability  $P(X \geq x)$  of observing a value of the random variable  $X$  above a threshold  $x$ , as a function of  $x$ )

of the observed samples collected from all five runs at QSS are illustrated in Figure 2.B. Both distributions display striking heavy tails relative to a fitted half-normal distribution. The CCDFs are instead fit well by shifted power-laws of the form

$$P(X \geq x) = x_s^\theta (x + x_s)^{-\theta}, \quad (1)$$

for some shifts  $x_s$  and power-law exponents  $\theta$ . For  $|\Delta U_-|$  we find  $\theta = 4.21 \pm 0.59$  (where the standard deviation is determined from the five runs) and  $x_s = 90 \pm 27 k_B T$ ; for  $\Delta U_+$  we find  $\theta = 11.14 \pm 3.04$  and  $x_s = 339 \pm 149 k_B T$ . Thus  $|\Delta U_-|$  has much shallower tails as well as an earlier onset of power-law behavior than  $\Delta U_+$ .

We also measured the non-Gaussian parameter

$$\eta = \frac{\langle x^4 \rangle}{3\langle x^2 \rangle^2} - 1, \quad (2)$$

where  $\langle x^m \rangle$  is the  $m^{\text{th}}$  moment about zero; for a half-normal distribution  $\eta = 0$ , and  $\eta > 0$  quantifies heavy-tailedness. We find  $\eta = 11.37 \pm 5.37$  for  $\Delta U_-$  and  $\eta = 1.96 \pm 0.58$  for  $\Delta U_+$ . This, along with the shallower tails of the fitted shifted power-laws, indicates greater deviation from Gaussianity for energy release compared to energy accumulation. These results support the picture that energy accumulation occurs comparatively slowly and is released via large, sudden events.

We next analyze the temporal correlations of  $U(t)$  at QSS. A self-affine stochastic time series  $G(t)$ , for which  $G(t)$  and  $|\zeta|^{Ha} G(t/\zeta)$  have the same statistical properties for any scaling parameter  $\zeta$ , has a power spectral density  $S(f)$  exhibiting a power-law dependence on frequency  $f$ :

$$S(f) \propto f^{-\beta}, \quad (3)$$

where the spectral exponent  $\beta$  is the persistence strength, related to the color of the signal. We find  $\beta = 1.72 \pm 0.02$  for  $U(t)$  as shown in Figure 2.C, painting  $U(t)$  as a pinkish brown signal; thus  $U(t)$  is non-stationary and has temporally anti-correlated increments  $\Delta U$  [25, 26]. Self-affine time series further obey the theoretical relationship  $\beta = 2Ha + 1$  when  $1 \leq \beta \leq 3$ , where  $Ha$  is the Hausdorff exponent determined from the scaling of the semivariogram

$$\gamma(\tau) = \frac{1}{2} \overline{(G(t + \tau) - G(t))^2} \sim \tau^{2Ha}, \quad (4)$$

and where the bar represents temporal averaging [27, 28]. We find that this relationship is satisfied by  $U(t)$ , as shown in Figure 2.D, yielding  $Ha = 0.36 \pm 0.01$  and confirming that  $U(t)$  is self-affine. Such non-Markovian and self-affine time series and

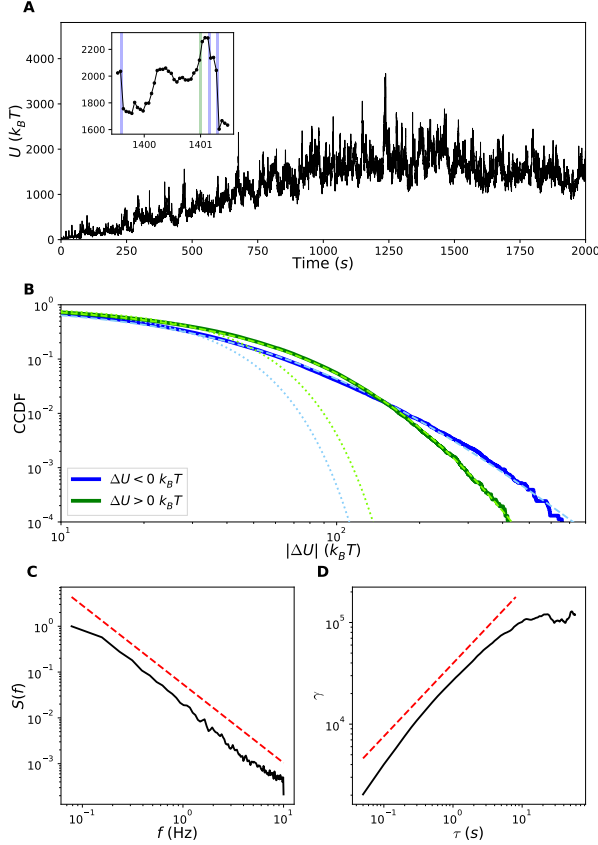


FIG. 2. Statistics of  $\Delta U$ . **A**: Trajectory of the network's mechanical energy  $U(t)$  for condition  $C_{3,3}$ . Inset: A blow-up of the trajectory to show instances of rare events ( $|\Delta U| > 100 k_B T$ ) of energy release (blue) and accumulation (green). **B**: CCDFs of  $|\Delta U_-|$  (blue) and  $\Delta U_+$  (green) collected from five runs when the system is at QSS after 1000 s. Dotted lines in lighter colors represent fits to the data of a half-normal CCDF, and dashed lines represent fits of shifted power-laws. **C**: The normalized power spectral density of  $U(t)$  for a single run at QSS from which the spectral exponent  $\beta = 1.72$  is determined by fitting a power-law, shown offset in red. **D**: The semivariogram obeys the scaling relationship  $\gamma \sim \tau^{2Ha}$  over the scaling range. We determined  $Ha = 0.36$  from the theoretical relationship for self-affine time series  $\beta = 2Ha + 1$  using  $\beta = 1.72$ . This result for  $Ha$  is plotted as the offset red line, indicating reasonable agreement of the data with this relationship.

spatial patterns commonly arise in various complex geophysical processes (e.g. the temporal variation of river bed elevation), illustrating further qualitative similarities between the cytoskeleton and earth systems [29, 30].

## B. Cytoquakes entail global filament displacements and tension homogenization

In Figure 3 we show that rare large events of energy accumulation correspond to a greater than usual number of myosin motor steps whereas rare large events of energy release correspond to greater than usual total displacement of the actin filaments and a slightly greater number of linker unbinding events. These large total displacements do not come from highly localized motions, and instead depend on many filaments each being displaced more than usual, as shown in Figure 4. This agrees with the notion of cytoquakes as global structural rearrangements of the network. We also observe cytoquakes to induce a spatial homogenization of the tension sustained by the network, as measured by changes in the Shannon entropy  $H(t)$  of the spatial tension distribution (see Methods). Thus cytoquakes tend to involve a spreading out of localized tension.

Previous experimental definitions of cytoquakes have focused on cytoskeletal displacements, which we observe correlates with large releases of energy [6, 7]. The absolute size of the displacements during these 0.05 s long intervals observed here is not very large, as each filament moves only on the order of a few *nm*. We find this estimate of speed to be consistent in order of magnitude with corresponding *in vitro* measurements [31]. Perhaps during cytoquakes, these displacements are collectively coordinated in such a way as to drastically reduce the energy; we later show that these displacements correspond to preferential motion along the soft vibrational modes of the network.

## C. Process of energy accumulation and release is subcritical

Technical definitions of what constitutes SOC behavior are not universally agreed upon, but we follow the definition of Ref. 28 which states that SOC systems must have event size distributions that tend to a power-law in the limit of an infinite system size, and a temporal signal that integrates a pink noise process, giving  $\beta = 3$  for the signal. The observed distribution of  $|\Delta U_-|$  for this system size is a shifted power-law and has  $\beta = 1.72$ , and thus appears not to be SOC but rather subcritical. To confirm this, we studied the dependence of the distribution of  $|\Delta U_-|$  on the system size (see Methods). In Figure 5 we display the CCDFs of  $|\Delta U_-|$  for these simulations, showing the approach to Gaussianity as system size increases. This trend is quantified using the non-Gaussian parameter  $\eta$ , which exhibits, curiously, a power-law decay with the system volume

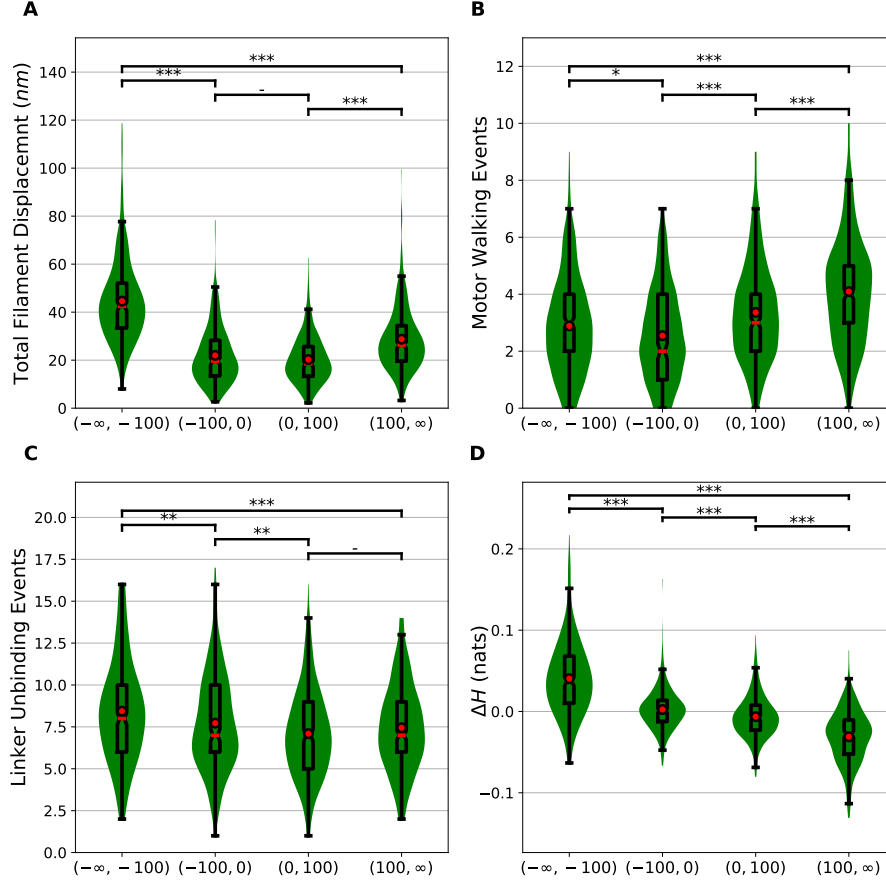


FIG. 3. Distinguishing features of cytoquakes. **A**: Differences in the total filament displacement between simulation cycles for which  $\Delta U$  is less than  $-100 k_B T$ , cycles for which  $\Delta U \in (-100 k_B T, 0 k_B T)$  (where a random sub-sample of all events is taken to be roughly equal to the number of events for which  $\Delta U < -100 k_B T$ ,  $n \sim 300$ ), cycles for which  $\Delta U \in (0 k_B T, 100 k_B T)$  (where a similar sub-sample is taken), and finally cycles for which  $\Delta U$  is greater than  $100 k_B T$ . To compare these distributions, the two-sided  $p$ -value of the Wilcoxon rank-sum test between pairs of cycle types is reported as being either not significant: - ( $p \geq 0.05$ ), significant at level 1: \* ( $p < 0.05$ ), at level 2: \*\* ( $p < 0.01$ ), or at level 3: \*\*\* ( $p < 0.001$ ). The total filament displacement is computed as the sum over all filaments of the distance between a filament at time  $t + \delta t$  and that filament at time  $t$ . The calculation of distance between filaments is described in the Supplementary Material. In these combination violin and box-and-whisker plots, the red circle represents the mean, the red bar represents the median, and the notches in the box represent the 95% confidence interval of the median. This data is collected from one run of condition  $C_{3,3}$  at QSS. **B**: Differences in the number of motor walking events between the different cycle types as just described. **C**: Differences in the number of  $\alpha$ -actinin unbinding events between the different cycle types. **D**: Differences in the Shannon entropy of the spatial distribution of network tension.

V. Thus, we conclude that cytoskeletal networks for these physiological conditions display subcritical dynamics. The approach to Gaussianity can be understood as a manifestation of the central limit theorem applied to increasing amounts of subcritical actomyosin. The heavy tails of  $\Delta U_+$  indicate that the driving in the system may not be sufficiently slow to yield SOC behavior, and the non-conservative transfer of mechanical energy between network components due to dissipation may also play a role [8, 32–34]. Notably, recent work has indicated that in com-

plex systems which may be continuously parameterized to the point where they exhibit SOC, it is possible to make predictions of avalanche sizes only in the non-critical (i.e. non-conservative coupling) regime [34]. It remains to be explored whether tuning various parameters of cytoskeletal networks can bring about true SOC.

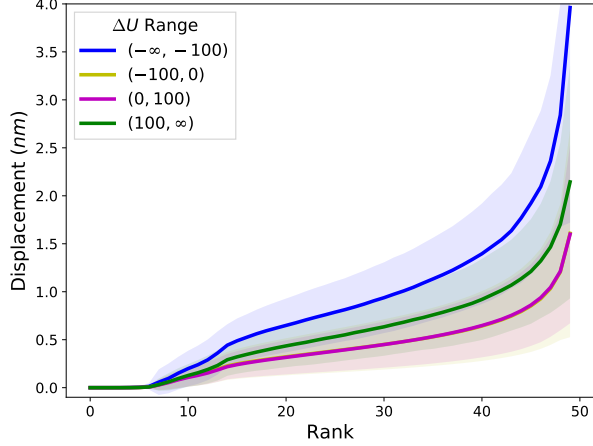


FIG. 4. Rank-size distribution of the displacements experienced by each of the 50 filaments during simulation cycles when  $\Delta U$  is in different ranges. For each cycle, the filaments are ranked according to their displacement and these ranks are plotted against the corresponding displacement. The average and standard deviation of these rank-displacement curves are taken over each cycle in a given category. Interestingly, the curves for the categories  $\Delta U \in (-100 k_B T, 0 k_B T)$  and  $\Delta U \in (0 k_B T, 100 k_B T)$  are almost exactly coincident.

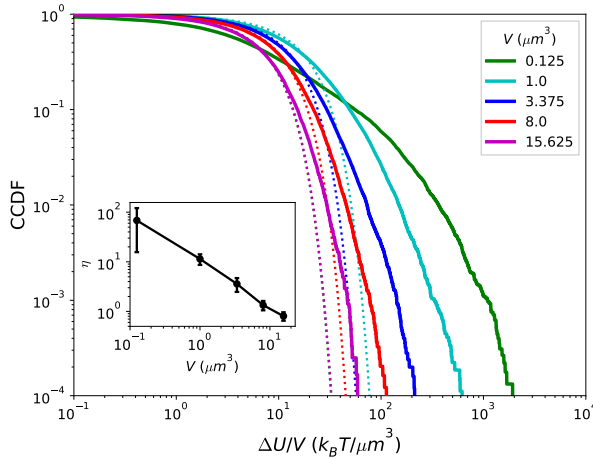


FIG. 5. CCDFs of  $|\Delta U|$  normalized by the system volume  $V$  for increasing system sizes. Data is collected from 5 runs of each condition, from 300 to 800 s. Half-normal CCDFs are fit to the data and shown as dotted lines. The half-normal fits of both the  $0.125 \mu m^3$  and  $15.625 \mu m^3$  conditions happen to be coincident. Inset: the non-Gaussian parameter  $\eta$  is plotted for each distribution with uncertainty taken over the different runs, showing power-law dependence on  $V$ .

#### D. Normal mode decomposition probes network's mechanical state

Having described the statistics of the increments  $\Delta U$ , we next aim to connect the occurrence of cytoquakes, defined as large values of  $|\Delta U|$ , to the cytoskeletal network's mechanical stability. To this end we implemented a method to compute the Hessian matrix  $\mathcal{H}$  of the mechanical energy function  $U$  (see Methods). The eigen-decomposition  $\mathbf{\Lambda} = \{\lambda_k\}_{k=1}^{3N}$  of  $\mathcal{H}$  is the primary object of our focus due to its relation to the mechanical stability of the cytoskeletal network. The eigenvectors  $\mathbf{v}_k$  are the normal vibrational modes of the network, and the eigenvalues  $\lambda_k$  indicate the stiffness ( $|\lambda_k|$ ) and stability ( $\text{sgn}(\lambda_k)$ ) of the corresponding mode. Such a vibrational mode is illustrated in Figure 1 (see also SI Movies 2-5). We draw inspiration for studying  $\mathbf{\Lambda}$  for cytoskeletal networks from several sources: in single-molecule molecular dynamics studies, the saddle-points of  $U$  (i.e. points in the landscape with some imaginary frequencies) are associated with transition states [35, 36]; in simulations of glass-forming liquids, the instantaneous normal mode spectrum allows inference about proximity to the glass transition [37–39]; in deep learning models for predicting earthquake aftershock distributions, it was found that certain metrics also related to stability (e.g. the von-Mises criterion) are informative model inputs [40, 41].

As Hessian analysis has not to our knowledge previously been performed for cytoskeletal networks, we first digress to describe some interesting observed trends of metrics defined on  $\mathbf{\Lambda}$  before turning to our main purpose, which is to use  $\mathbf{\Lambda}$  as the input of a machine learning model to forecast cytoquake occurrence.

We find that the mean value  $\langle r_k \rangle$  (which measures delocalization of the stable modes at QSS, see Methods) varies non-monotonically with myosin motor concentration  $[M]$  and  $\alpha$ -actinin concentration  $[\alpha]$  (Figure 6.C). To understand this trend we implemented a mapping from the cytoskeletal network into a graph and measured its mean node connectivity, a purely topological measure of network percolation (see Methods). Revealingly, the mean node connectivity correlates closely with  $\langle r_k \rangle$  for the stable modes across the various conditions  $C_{i,j}$  (Figure 6.D). We also find the number of connected components of  $\mathcal{H}$  and of the graph's adjacency matrix to match for most time points, supporting this connection between network topology and stable mode delocalization. Intermediate concentrations of myosin motors enhance the network percolation, but as  $[M]$  continues to increase the motors act to disconnect cross-linked network structures causing the mean



node connectivity and  $\langle r_k \rangle$  to decrease.

We observe that as a network contracts and becomes percolated during the process of myosin-driven self-organization, the stable modes steadily delocalize ( $\langle r_k \rangle$  increases) and stiffen (the geometric mean  $\langle \lambda_k \rangle_g$  increases), as shown in Figures 6.E and Figures 6.F. During this process we also witness a qualitative change in the level spacing statistics of the very soft and delocalized modes ( $\lambda_k < 10 \text{ pN/nm}$ ,  $r_k > 100$ ) from a Poisson to a Wigner-Dyson distribution (Figure 7). This indicates that in the percolated state these vibrational modes interact and exhibit level repulsion, similar to soft particles near the jamming transition [7, 11, 42, 43]. Future studies may reveal further similarities between these systems and other marginally stable solids [44, 45].

### E. Cytoquakes exhibit enhanced displacement along soft modes

As a final application of Hessian analysis before employing it to forecast cytoquakes, we determined the projections of the cytoskeletal network's displacements onto the vibrational normal modes  $\{\mathbf{v}_k\}_{k=1}^{3N}$  to discover additional distinguishing features of cytoquake events (see Methods). The mean ratio  $n_{\text{soft}}/n_{\text{stiff}}$  (which measures the tendency to displace along soft rather than stiff modes) for different simulation cycle types are displayed in the inset of Figure 8, showing enhanced displacements along soft modes during cytoquakes. We also considered the effective stiffness (or projection-weighted eigenvalue)  $\lambda_P$  experienced during the displacement **d**. In Figure 8 we display a scatter plot of the pairs  $\Delta U$ ,  $\lambda_P$  measured during QSS for a run of condition  $C_{3,3}$ , along with a kernel density estimate of their joint probability density function (PDF). The structure of the joint PDF shows that  $\lambda_P$  during cytoquake events is almost always soft, whereas for all other simulation cycles  $\lambda_P$  could be soft or stiff with similar probabilities. Based on this analysis, we conjecture that in order to achieve large global rearrangements during cytoquakes, cytoskeletal networks take the “path of least resistance” by deforming primarily along the soft modes.

### F. Mechanical instability precedes cytoquakes

Can the eigen-decomposition of the Hessian matrix be used to forecast cytoquake occurrence? Intuition suggests that, in analogy with the connection between imaginary frequencies (i.e. unstable modes) and molecular transition states, the vibrational modes of the cytoskeletal network may con-

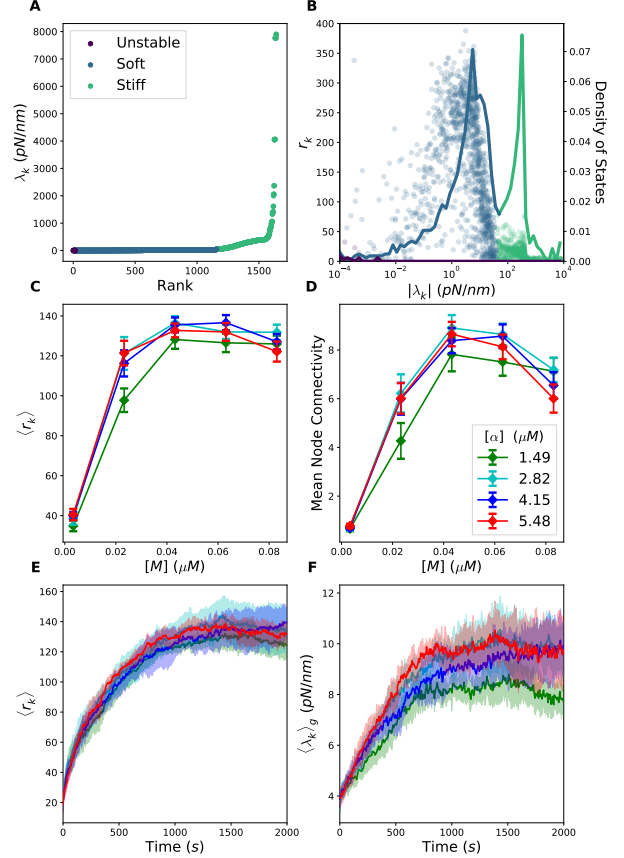


FIG. 6. Metrics defined on Hessian eigen-decomposition. **A:** Ordered eigenspectrum  $\{\lambda_k\}_{k=1}^{3N}$  at a QSS time point for condition  $C_{3,3}$ . **B:** Scatter plot of the pairs  $|\lambda_k|, r_k$  (circles) plotted against the density of states (solid lines), i.e. the proportion of eigenvalues between  $\lambda$  and  $\lambda + d\lambda$ . **C:** The mean value at QSS of  $\langle r_k \rangle$  for the stable modes for various conditions  $C_{i,j}$ . The conditions  $C_{1,j}$  with low linker concentrations are not visualized as these networks did not percolate and obscure visualization for the remaining conditions. The mean is taken over the last 500 s and over different runs. **D:** The mean value of the mean node connectivity for various conditions. **E:** Trajectories of  $\langle r_k \rangle$  of the stable modes as the network self-organizes for the conditions  $C_{2,3}$ ,  $C_{3,3}$ ,  $C_{4,3}$ , and  $C_{5,3}$ , with the mean and standard deviation taken over the different runs. **F:** Similar trajectories of  $\langle \lambda_k \rangle_g$  of the stable modes.

tain information that a large structural rearrangement is poised to occur. To test this idea, and without detailed *a priori* knowledge about which features in  $\mathbf{\Lambda}$  would be informative, we implemented a machine learning (ML) model using the eigen-decomposition as the input and outputting the predicted probability  $p$  of observing a large event of energy release (defined as  $\Delta U < -100 k_B T$ ) occurring within the next  $t_W = 0.15$  seconds (see Methods). We resorted to using a high-dimensional ML model

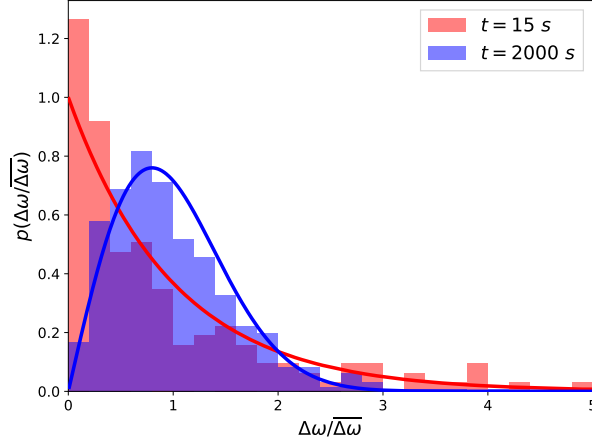


FIG. 7. Histograms of the level spacings  $\Delta\omega = \omega_{k+1} - \omega_k$ , where  $\omega_k = \sqrt{\lambda_k}$  are ordered so that  $\omega_k$  increases as  $k$  increases, normalized by their average  $\Delta\omega$  for the very soft ( $\lambda_k < 10$  pN/nm) and delocalized ( $r_k > 100$ ) vibrational modes at different times of a run of condition  $C_{3,3}$ . The Poisson distribution  $p(\Delta\omega/\Delta\omega) = e^{-\Delta\omega/\Delta\omega}$  and the Wigner-Dyson distribution  $p(\Delta\omega/\Delta\omega) = \frac{\pi}{2}(\Delta\omega/\Delta\omega)e^{-\frac{\pi}{4}(\Delta\omega/\Delta\omega)^2}$  are plotted as red and blue solid lines. This transition in distributions signifies that in the percolated network at 2000 s the frequencies of these modes are no longer randomly spaced and begin to interact, exhibiting level repulsion for small  $\Delta\omega/\Delta\omega$ .

after it was found that several simple features in the eigenspectrum which we believed might reflect mechanical stability (for instance the value of the smallest positive eigenvalue) did not by themselves significantly correlate with cytoquake occurrence.

We found that the Hessian eigenspectrum  $\{\lambda_k(t)\}_{k=1}^{3N}$  contains sufficient information to forecast cytoquake occurrence with significant accuracy, with an AUC (which measures model performance) of 0.81 when using data from a single run of condition  $C_{3,3}$  (Figure 9.C) and of 0.70 when using data from all five runs. To gain insight into broadly which features carry the most predictive information, we varied the model by including different subsets of predictors as the input, as shown in Figure 9.D Keeping only the eigenvalues of the soft modes does not harm performance, giving an AUC of 0.71, while keeping only the stiff modes does harm performance, giving an AUC of 0.68. Performance slightly improves upon augmenting the input with the inverse participation ratios  $\{r_k(t)\}_{k=1}^{3N}$ . Interestingly, we also found that a logistic regression model using only the mechanical energy  $U(t)$  as an input feature performs quite well, reminiscent of the debate concerning one neuron vs. deep learning models of earthquake aftershock prediction [40, 41]. This logis-

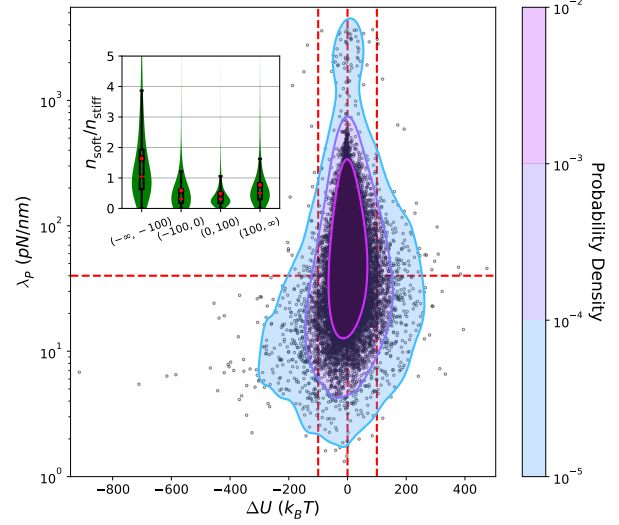


FIG. 8. Scatter plot of the pairs  $\Delta U, \lambda_P$  measured during QSS for a run of condition  $C_{3,3}$ . From these points, a Gaussian kernel density estimate of the joint PDF (treating  $\lambda_P$  on a log-scale) is constructed and shown as a contour plot. Red guidelines demarcate regions of interest. Inset: Combination violin and box-and-whisker plots showing the ratio  $n_{\text{soft}}/n_{\text{stiff}}$  for different categories of simulation cycles (c.f. Figure 3). The Wilcoxon rank-sum test indicates significant (\*\*\*) differences in the distributions for all pairs of cycles types. The inset is not blocking any of the scatter plot data.

tic regression model has learned an optimal cutoff for  $U$  that indicates instability and likely cytoquake occurrence. We may seemingly conclude that the ML model using the Hessian eigenspectrum as an input has merely learned what the mechanical energy is, however we find that by far the best performance results from combining  $\{\lambda_k(t)\}_{k=1}^{3N}$ ,  $\{r_k(t)\}_{k=1}^{3N}$ , and  $U$  in the ML model, reaching an AUC of 0.79. This suggests that the learned features of the Hessian eigenspectrum are not redundant given  $U$ , i.e. that their mutual information is low. Finally, we found that prediction of large positive increments ( $\Delta U > 100 k_B T$ ) is also possible, though with poorer performance than of the negative increments.

Taken together, these results show that the stiffness and delocalization of the soft vibrational modes of the cytoskeletal network along with its current mechanical energy reflect the propensity of the system to suddenly undergo a large change in mechanical energy. Apparently there is a signature in the Hessian eigenspectrum that prefigures large jumps in the mechanical energy landscape being explored during stochastic chemical dynamics.



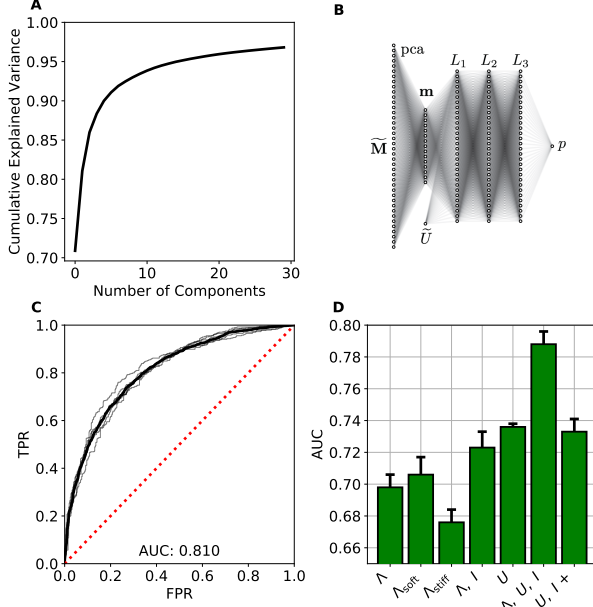


FIG. 9. Implementation details and results of ML model. **A:** Cumulative explained variance from PCA of the  $\sim 1,600$  eigenvalues  $\{\lambda_k(t)\}_{k=1}^{3N}$ . **B:** Schematic depiction of the feed-forward neural network architecture. The numbers of nodes in each layer are not to scale. The original input vector  $\vec{M}$ , which includes either just  $\{\lambda_k\}_{k=1}^{3N}$  or also  $\{r_k\}_{k=1}^{3N}$  after rescaling, is reduced to the low-dimensional vector  $\vec{m}$ , to which the rescaled energy  $\tilde{U}$  is optionally included. The neural network consists of the three hidden layers  $L_1$ ,  $L_2$ , and  $L_3$ , outputting the cytoquake probability  $p$ . **C:** ROC curves for the model using only  $\{\lambda_k\}_{k=1}^{3N}$  as input and trained on a single run of condition  $C_{3,3}$ , with 5 realizations of the stochastic batch network training and their average shown. The ROC curve of a random model is plotted as the red dotted line. **D:** Bar plot indicating the AUC of ROC curves using different combinations of inputs for the model trained on data collected from all runs of condition  $C_{3,3}$ . From left to right, the labels indicate that the model inputs are:  $\{\lambda_k\}_{k=1}^{3N}$ ;  $\{\lambda_k | 0 \leq \lambda_k < \lambda_T\}$ ;  $\{\lambda_k | \lambda_T \leq \lambda_k\}$ ;  $\{\lambda_k\}_{k=1}^{3N}$  and  $\{r_k\}_{k=1}^{3N}$ ;  $U$ ;  $\{\lambda_k\}_{k=1}^{3N}$ ,  $\{r_k\}_{k=1}^{3N}$ , and  $U$ ;  $\{\lambda_k\}_{k=1}^{3N}$ ,  $\{r_k\}_{k=1}^{3N}$ , and  $U$  with forecasting done for large positive increments  $\Delta U > 100 k_B T$ .

### III. DISCUSSION

We have presented evidence which supports the following picture of active cytoskeletal network self-organization: cytoskeletal networks explore a rugged mechanical energy landscape in a self-affine random walk characterized by occasional, sudden jumps out of metastable configurations [44, 46]. These jumps entail significant dissipation of mechanical energy and are typically accomplished by an avalanche-like process of spreading destabilization, resulting

in a global structural rearrangement. These motions have large projections along the soft, delocalized vibrational modes, and furthermore, properties of these modes can be used to predict when such relaxation events are about to occur. We have argued for this connection between vibrational modes and avalanche-like mechanical relaxation events based on analogy with single-molecule studies, and a ML model has proven the existence of correlations between the two while, for now, obscuring further mechanistic details due to a lack of interpretability. Confirming and filling in the details of this picture is deserving of future research effort, not least because a more detailed understanding of mechanical dissipation by cytoskeletal networks will help to advance certain traction-based experimental techniques [13].

Our novel application of ML to dynamically forecast large remodeling events has revealed that mechanical information of the network alone can be sufficient to make short-term predictions of behavior, without any input on the current chemical propensities. This is quite surprising given the inherent randomness of the chemical reactions (e.g. motor walking and linker unbinding) which drive the network through the mechanical energy landscape. While this mechanical information is not enough to make quantitative predictions of  $\Delta U$  (as in a regression model), it reliably distinguishes “precipitous” network configurations which with high probability will induce a large relaxation event. The ability of ML to overcome stochastic noise in pattern detection is well-served to the problem of establishing the existence of such precipitous configurations. In future studies it will be of interest to investigate more deeply into these configurations’ structural properties.

In order to simplify matters as much as possible we have focused on a minimal system (i.e. relatively small networks comprising just three types of molecules), which is nevertheless sufficient to produce cytoquakes. However, interesting new phenomena may emerge at larger length scales, where one may find extended unstable interfaces similar to faults [6, 47]. At these larger scales, the self-similar organization of the cytoskeleton may also affect the heavy-tailed distributions of event sizes. Recent experiments have discovered fractal patterning of cortical actin networks *in vivo*, which has been argued to give rise to anomalous diffusion of membrane proteins via cytoskeleton-membrane interactions [48]. It has also been shown in certain forest-fire models that self-similarly “pre-structured” systems exhibit dependence of the power-law exponent on the fractal dimension of the system [28, 49, 50]. Thus, it may be the case that the fractal dimension of the cytoskeleton modulates the frequency and magnitudes of cy-

toquakes which result from the inherent driven, dissipative dynamics, similarly to in the earth [27, 51–53]. Continued exploration of the recently discovered and surprising similarities between the active cytoskeleton and SOC earth systems promises to reveal key insights into the mechanics of cells.

## IV. METHODS

### A. Actomyosin networks

We focus on a subsystem of the full cytoskeleton called an actomyosin network. These consist of semi-flexible actin filaments and associated proteins, including active molecular motors (e.g. minifilaments of non-muscle myosin IIA) and passive cross-linkers (e.g.  $\alpha$ -actinin). The actin filaments hydrolyze ATP molecules in a directed polymerization process which reaches a steady state called “treadmilling” [54]. The myosin minifilaments ( $\sim 200$  nm in length) transiently bind to pairs of actin filaments and also hydrolyze ATP as fuel to walk along the filaments, generating motion and mechanical forces. The cross-linkers ( $\sim 35$  nm) bind more stably to nearby filaments, serving to transmit the force produced by motors and to both store and through unbinding dissipate the resulting energy, heating the cell [13, 23, 55–59]. We omit other associated proteins, such as the branching agent Arp2/3, finding that our minimal system is sufficient to produce cytoquake behavior, although it has recently been discovered that branching acts to enhance avalanche-like processes [60]. The rates of myosin motor walking and unbinding as well as of cross-linker unbinding depend on the forces sustained by the molecules, giving rise to non-linear coupling between the mechanical state of the cytoskeleton and its chemical propensities [61, 62]. An actomyosin network as represented in simulation is visualized in Figure 1.

### B. Experimental conditions

We performed MEDYAN simulations of small cytoskeletal networks consisting of 50 actin filaments in  $1 \mu\text{m}^3$  cubic boxes with varying concentrations of  $\alpha$ -actinin cross-linkers ( $[\alpha]$ ) and of NMIIA minifilaments ( $[M]$ ). Five concentrations of  $\alpha$ -actinin (ranging from 0.17 to  $5.48 \mu\text{M}$ ) and five concentrations of myosin minifilaments (ranging from 0.003 to  $0.08 \mu\text{M}$ ) were used with a constant G-actin monomer concentration of  $13.3 \mu\text{M}$ , in the regime of physiological concentrations [63]. This led to a steady state filament length distribution with mean  $0.48 \mu\text{m}$  and standard deviation  $0.26 \mu\text{m}$ . We label these condi-

tions  $C_{i,j}$ , where  $i = 1, \dots, 5$  represents the rank of the cross-linker concentration and  $j = 1, \dots, 5$  represents the rank of the myosin motor concentration. The length of the simulation cycle  $\delta t$  was chosen as  $0.05$  s. Five runs of each condition  $C_{i,j}$  were simulated. The parameterization (i.e. choice of mechanical constants, reaction rates, etc.) of these simulations was chosen to closely match *in vivo* cytoskeletal systems and is described in the Supplementary Material.

### C. Entropy of spatial tension distribution

The simulation volume of  $1 \mu\text{m}^3$  is discretized into  $10^3$  cubic voxels, each  $0.1 \mu\text{m}$  in linear dimension. Let  $i, j, k = 1, \dots, 10$  index these voxels, which are an analysis tool and not related to the reaction-diffusion compartments used in MEDYAN. After each simulation cycle, the mechanical components of the cytoskeletal network (i.e. the filament cylinders, the myosin motors, and the passive cross-linkers) are each under some compressive or tensile force  $T_n$ , where  $n$  indexes the mechanical component. There are other mechanical potentials involving these components, but we focus here only on the tensions  $T_n$ . Each mechanical component has a center of mass  $\mathbf{r}_n$ , and we introduce the indicator function  $\chi_{ijk}(\mathbf{r}_n)$  which is equal to 1 if  $\mathbf{r}_n$  is inside voxel  $i, j, k$  and 0 otherwise. The total tension magnitude inside voxel  $i, j, k$  is

$$|T|_{ijk} = \sum_n |T_n| \chi_{ijk}(\mathbf{r}_n). \quad (5)$$

The discrete non-negative scalar field  $|T|_{ijk}$  is converted to a probability distribution  $p_{ijk}$  by normalization:

$$p_{ijk} = \frac{|T|_{ijk}}{\sum_{ijk} |T|_{ijk}}. \quad (6)$$

Finally, we introduce the Shannon entropy of this distribution at time  $t$  as

$$H(t) = - \sum_{ijk} p_{ijk}(t) \ln p_{ijk}(t). \quad (7)$$

The units of  $H$  are nats, and large values indicate a homogeneous spatial distribution of tension magnitudes throughout the network. Reported trends using this metric are essentially independent of the discretization length.

### D. Finite-size scaling study

Holding the concentrations of all chemical species for condition  $C_{3,3}$  fixed, we performed simulations

using cubic volumes with side lengths ranging from 0.5 to 2.5  $\mu\text{m}$ . Larger systems reach QSS at later times, and our simulations of larger systems did not reach QSS in the allotted computational time. As a result, we collected samples of  $|\Delta U_-|$  for these systems on the approach to QSS, from 300 to 800  $s$ , once the networks had all nearly fully percolated (i.e. nearly all filaments belonged to a single component connected by cross-linkers), trusting that the relevant scaling behavior could still be observed.

### E. Constructing the Hessian matrix

In MEDYAN, semi-flexible filaments are represented as a connected sequence of thin cylinders whose joined endpoints (i.e. hinges) are called beads. The set of potentials defining the mechanical energy of the filaments and associated proteins is outlined in the Supplementary Materials. The mechanical energy  $U$  is a function of these beads' positions, and elements of the Hessian matrix are defined as

$$\mathcal{H}_{i\mu,j\nu} = \frac{\partial^2 U}{\partial x_{i\mu} \partial x_{j\nu}} = -\frac{\partial F_{i\mu}}{\partial x_{j\nu}} = -\frac{\partial F_{j\nu}}{\partial x_{i\mu}}, \quad (8)$$

where  $x_{i\mu}$  is the  $\mu^{\text{th}}$  Cartesian component of the position of the  $i^{\text{th}}$  bead. We have  $\mu = x, y, z$  and  $i = 1, \dots, N$  where  $N$  is the number of beads in the network, so  $\mathcal{H}$  is a square symmetric  $3N$ -dimensional matrix. The number of beads  $N(t)$  will change as filaments (de)polymerize; in these simulations, at QSS a single filament of length 0.5  $\mu\text{m}$  comprises  $\sim 10$  cylinders (11 beads), each  $\sim 50 \text{ nm}$  in length. After each mechanical minimization,  $\mathcal{H}(t)$  is constructed by numerically computing the derivatives on the right of Equation 8. The derivative  $\frac{\partial F_{i\mu}}{\partial x_{j\nu}}$  is found using a second-order central difference approximation by moving the  $j^{\text{th}}$  bead in the  $\pm\nu$  directions by a small amount and determining the changes in the force component  $F_{i\mu}$  [64]. Due to issues of numerical accuracy, we do not assume the symmetry of the matrix  $\mathcal{H}$ , but instead directly compute each component  $\mathcal{H}_{i\mu,j\nu}$  and then symmetrize the result:  $\frac{1}{2}(\mathcal{H}^T + \mathcal{H}) \rightarrow \mathcal{H}$ .

### F. Classifying vibrational modes

We distinguish between unstable, stable, soft, and stiff modes: for unstable modes  $\lambda_k < 0$ , for stable modes  $\lambda_k \geq 0$ , for soft modes  $0 \leq \lambda_k < \lambda_T$ , and for stiff modes  $\lambda_k \geq \lambda_T$ , where we define the threshold  $\lambda_T = 40 \text{ pN/nm}$  to discriminate between the twin peaks in the density of states (Figure 6.B). The set

$\{\lambda_k\}_{k=1}^{3N}$  is visualized with these modes labeled in Figure 6.A for a QSS time point of condition  $C_{3,3}$ . A very small number of unstable modes persist after each minimization cycle, the latter iterations stopping once the maximum force on any bead is below a threshold  $F_T$  (here 1  $\text{pN}$ ). Thus the minimized configurations are in fact saddle-points of  $U$ ; this is expected as it is known from the theory of minimizing loss functions that the ratio of saddle-points to true local minima increases exponentially with the dimensionality of the domain [65]. We expect that in the space of all possible network topologies (i.e. patterns of cross-linkers and motors binding to filaments), the energy landscape will be rugged, leading to the well-appreciated glassy dynamics of non-equilibrium cross-linked networks [44–46]. For a fixed topology, however, which is the result of the chemical reactions occurring during step 1) of the iterative simulation cycle, the energy landscape should be smooth (i.e. non-rugged) with respect to the beads' positions, with a single nearby local minimum being sought during mechanical minimization in step 3). The residual unstable modes are therefore thought to be an unimportant artifact of thresholded stopping in the conjugate-gradient minimization routine, and not representative of some physical feature of cytoskeletal networks. The observed quantitative dependence of the number of residual unstable modes on  $F_T$  supports this conclusion and is illustrated in the Supplementary Material.

### G. Representing network topology as a graph

We construct a graph to represent the cross-linker binding topology of cytoskeletal networks. Nodes in the graph correspond to actin filaments, and weighted edges (which may be thresholded and converted to binary edges in an unweighted graph) between nodes correspond to the number of cross-linkers connecting the pair of filaments. The mean node connectivity is defined as the average over all pairs of nodes in the unweighted graph of the number of edges necessary to remove in order to disconnect them, thus quantifying the typical number of force chains between filaments, or equivalently the extent of network percolation [66, 67].

### H. Metrics involving Hessian eigenspectrum

We quantify the number of degrees of freedom involved in a given normalized eigenvector  $\mathbf{v}_k$  using

the inverse participation ratio [37]:

$$r_k = \left( \sum_{i=1}^N \sum_{\mu=1}^3 (v_{k,i\mu})^4 \right)^{-1}. \quad (9)$$

If the eigenmode involves only one degree of freedom, then one component of  $\mathbf{v}_k$  will be one and the rest will be zero, and  $r_k = 1$ . On the other hand, if the eigenmode is evenly spread over all  $3N$  degrees of freedom, then each component  $v_{k,i\mu} = (3N)^{-1/2}$ , and  $r_k = 3N$ . In Figure 6.B we plot  $r_k$  for the unstable, soft, and stiff modes along with the density of states, showing that the soft modes involve many degrees of freedom while the stiff and unstable modes are comparatively localized.

Network displacements  $\mathbf{d}(t)$  were found by tracking the movement of each of the  $N(t)$  beads during simulation cycles. As a working approximation, beads that depolymerized during a cycle were assigned a displacement of 0, and beads that newly polymerized were not assigned elements in  $\mathbf{d}(t)$ . The  $3N$ -dimensional displacement vectors  $\mathbf{d}$  were then normalized to have unit length. We define the following quantities:

$$d_k = \mathbf{d} \cdot \mathbf{v}_k, \quad (10)$$

$$n_k = \frac{d_k^2}{r_k}, \quad (11)$$

and

$$\lambda_P = \sum_{k=1}^{3N} d_k^2 \lambda_k. \quad (12)$$

The  $d_k$  are the projections of  $\mathbf{d}$  onto the eigenmodes  $\mathbf{v}_k$ , which obey

$$\sum_{k=1}^{3N} d_k^2 = 1 \quad (13)$$

owing to the normalization of  $\mathbf{d}$  and  $\mathbf{v}_k$ . Thus the quantity  $d_k^2$  can be viewed as the weight of the displacement  $\mathbf{d}$  along the  $k^{\text{th}}$  eigenmode. Because the eigenmodes involve varying numbers of degrees of freedom, as quantified by  $r_k$ , we introduce  $n_k$  as the weight of the displacement along eigenmode  $k$  per degree of freedom involved in the eigenmode. We define  $n_{\text{soft}}$  and  $n_{\text{stiff}}$  as the mean of  $n_k$  over the eigenmodes belonging to the soft ( $0 \leq \lambda_k < 40 \text{ pN/nm}$ ) and stiff ( $\lambda_k \geq 40 \text{ pN/nm}$ ) subsets. We also define the effective stiffness  $\lambda_P$  as the weighted average of the eigenvalues  $\{\lambda_k\}_{k=1}^{3N}$  using the displacement weights  $d_k^2$ .

## I. Machine learning model

We performed principal component analysis (PCA) on the input vector to reduce its dimensionality, finding that only 30 dimensions (a compression factor of over 50) suffice to explain over 95% of the variance of  $\{\lambda_k(t)\}_{k=1}^{3N}$  (Figure 9.A). This reduced vector  $\mathbf{m}(t)$  is the input for a feed-forward neural network with three hidden layers, schematically illustrated in Figure 9.B. We provide details of the ML pipeline in the Supplementary Material.

A parameter  $p_T$  sets the threshold probability above which the model claims a cytoquake will occur. We evaluated our model by computing the area under the curve (AUC) for receiver operator characteristic (ROC) curves, which are the locus of points of true positive rate and false positive rate evaluated on the test data as the probability threshold  $p_T$  is varied from 0 to 1 (Figure 9.C). For a random model  $\text{AUC} = 0.5$ , while for a perfect model  $\text{AUC} = 1$ . The test data is balanced such that an equal number of cytoquake and non-cytoquake events are included, allowing the use of this AUC metric [68, 69].

## V. ACKNOWLEDGMENTS

We would like to thank A. Chandrasekaran, M. Girvan, H. Ni, Q. Ni, M. Nikolić, and H. Wu for helpful discussions and editing of the manuscript. This work was supported by the following grants from the National Science Foundation: 1632976, CHE-1800418, DMR-1506969, and PHY-1427654.

## SUPPLEMENTARY MATERIAL

### Description of MEDYAN Simulation Platform

A detailed description of the MEDYAN (Mechanochemical Dynamics of Active Networks) model can be found in Ref. 18, and additional extensions and applications of MEDYAN to study the dynamics of actomyosin networks are described in Refs. 8, 19–23. Here we briefly outline the relevant aspects of MEDYAN to facilitate understanding the results in this paper, and direct the reader to the above references for a more thorough introduction.

#### 1. Simulation Protocol

A MEDYAN simulation proceeds by iterating a cycle of four steps which propagate the chemical and mechanical dynamics forward while maintaining a tight coupling between the two. The steps are as follows:

1. Evolve system using stochastic chemical simulation for a time  $\delta t$ .
2. Compute the changes in the mechanical energy resulting from the reactions that occurred in step 1).
3. Mechanically equilibrate the network in response to the new stresses from step 2).
4. Update the reaction rates of force-sensitive reactions based on the new tensions from step 3).

This protocol reflects a separation of timescales between the slow chemical dynamics and the fast mechanical response, such that the mechanical subsystem is assumed to always remain near equilibrium and to adiabatically follow the chemical changes in the network. As argued in Ref. 18, supported using experimental evidence from Refs. 55, 70, and 71, this timescale separation holds for typical cytoskeletal networks which experience localized force deformations with fast relaxation times compared to the typical waiting time between myosin motor walking steps and filament growth-induced deformations.

#### 2. Chemistry

In MEDYAN, diffusing chemical species are represented with discrete copy numbers belonging to several compartments, which form a regular grid comprising the simulation volume. The compartment size is chosen so that it may be assumed that inside the compartments the diffusing species are well-mixed, allowing the use of mass-action kinetics to determine their instantaneous propensities to participate in chemical reactions within compartments and diffusion events between adjacent compartments. The minimum Kuramoto length (i.e. the mean free diffusional path length of a reactive species before it participates in a chemical reaction) among the species sets this compartment size to ensure that the well-mixed assumption holds [72]. The diffusing chemical species may participate in local chemical reactions according to the copy numbers of the reactants in its compartment, or else it may jump to an adjacent compartment in a diffusion event with a propensity determined by its copy number in the original compartment [73]. The algorithm for stochastically choosing which event (including local reactions or jumps between compartments) will occur next is the Next Reaction Method, an accelerated variant of the Gillespie algorithm [73, 74]. These are Monte Carlo methods which randomly select both the time to any next event and which event will occur at that time in accordance with each event’s instantaneous propensity.

The user specifies the different chemical species and the reactions that they participate in. Several types of reactions are possible. Regular reactions involve only diffusing species (e.g. the conversion of ADP-bound to ATP-bound G-actin monomer). Polymerization reactions result in the subtraction of a diffusing monomer from the local compartment and its conversion into a filament species, and depolymerization reactions do the opposite. Filaments in MEDYAN’s have definite spatial coordinates, rather than the compartment-level description of the diffusing species’ positions. This network of spatially resolved filaments is overlaid on the compartment grid, so that sections of filaments are able to react with diffusing species according to their local copy numbers. In addition, filaments have mechanical properties which will be discussed in the next section. A filament may react with a diffusing species such as a cross-linker (e.g.  $\alpha$ -actinin), branching (e.g.

Arp2/3), or molecular motor (e.g. NMIIA). Binding reactions involve a discrete set of binding sites along the filament, and they stochastically occur as chemical reaction events according to the number of those binding sites and the local copy number of diffusing binding molecules. A bound molecular motor may participate in a walking reaction, which causes it to move one of its ends to an adjacent binding site, stretching the motor and generating forces. Other reactions not used in this paper but encompassed by MEDYAN include filament nucleation, filament destruction, filament severing, and filament branching reactions.

### 3. Mechanics

The mechanical energy  $U$  of networks in MEDYAN is a function of the positions of the filament beads and the lengths of the molecules bound to the filaments. There are also potentials describing a branched filament's energy which are not included in this paper. Filament beads mark the joined end points (i.e. hinges) of the cylinders comprising the filament. Individual cylinders can stretch but not bend, but a bending energy term is included for pairs of adjacent cylinders. The energy term for the stretching of cylinders is

$$U_{\text{str}} = \frac{1}{2} K_{\text{fil, str}} (l - l_0)^2, \quad (14)$$

where  $l = \|\mathbf{r}_{i+1} - \mathbf{r}_i\|$  is the length of the cylinder whose beads are at positions  $\mathbf{r}_{i+1}$  and  $\mathbf{r}_i$ ,  $l_0$  is the cylinder's equilibrium length, and  $K_{\text{str}}$  is the spring constant of this harmonic potential. The energy term for the bending of adjacent cylinders is

$$U_{\text{bend}} = \epsilon_{\text{bend}} (1 - \cos(\theta_{i,i+1})), \quad (15)$$

where  $\epsilon_{\text{bend}}$  parameterizes the strength of the interaction and  $\theta_{i,i+1}$  is the angle between the cylinders. Molecules bound to pairs of filaments (e.g.  $\alpha$ -actinin and NMIIA) of stretched length  $l_{\text{bound}}$  have a harmonic stretching energy term:

$$U_{\text{bound, str}} = \frac{1}{2} K_{\text{bound, str}} (l_{\text{bound}} - l_{\text{bound}}^0)^2, \quad (16)$$

where the subscript “bound” indicates that the variables and parameters are specific to the bound molecule. An excluded volume interaction is included to prevent cylinders from overlapping. The analytical formula for this interaction is complicated but can be expressed as a double integral over the two lengths of the participating cylinders  $i$  and  $j$ :

$$U_{\text{vol, ij}} = K_{\text{vol}} \int_0^1 \int_0^1 \frac{ds dt}{|\mathbf{r}_i(s) - \mathbf{r}_j(t)|^4}, \quad (17)$$

where  $\mathbf{r}_i(s) = \mathbf{r}_i + s(\mathbf{r}_{i+1} - \mathbf{r}_i)$  is the position along the  $i$  cylinder, which is parameterized by a variable  $s$  running from 0 to 1 along the cylinder's length. These positions  $\mathbf{r}_i(s)$  are also therefore functions of the cylinders' bead positions,  $\mathbf{r}_i$  and  $\mathbf{r}_{i+1}$ . Finally, an exponentially decaying boundary repulsion term prevents the filaments from poking outside the simulation volume:

$$U_{\text{boundary}} = \epsilon_{\text{boundary}} e^{-d_i/\lambda}, \quad (18)$$

where  $\epsilon_{\text{boundary}}$  parameterizes the interaction strength,  $d_i$  is the distance from the boundary to the nearest endpoint of the  $i$  cylinder, and  $\lambda$  parameterizes the interaction screening length.

At the end of each chemical evolution cycle, the positions of the bound molecules and the filament beads will have changed due to the chemical reactions which occurred, displacing the system from near-equilibrium. The positions of the filament beads are then updated in a mechanical equilibration cycle by minimizing the total mechanical energy function  $U$ . This is accomplished using the conjugate-gradient minimization algorithm. The minimization procedure ends when the maximum net force remaining in the network is below a user-specified force tolerance  $F_T$ , as result of which the system returns to near mechanical equilibrium.



#### 4. Mechanochemical Coupling

An important facet of the dynamics of actomyosin networks is that the chemical reaction rates of the associated proteins depend on the forces they sustain: at high tension the myosin minifilaments will walk and unbind more slowly (stalling and catch-bond behavior) whereas the passive cross-linkers are modeled as unbinding more quickly under tension (slip-bond behavior) [61, 62]. These force-sensitive behaviors thus play the role of non-linearly coupling the mechanical state of the actomyosin network to its stochastic chemical dynamics.

The myosin motors used in MEDYAN are modeled after non-muscle myosin IIA (NMIIA), which exists in the cell as a minifilament consisting of tens of individual myosin heads. The chemical dynamics of the myosin minifilaments are based on the Parallel Cluster Model of Erdmann et al. [56, 75]. In this model, a myosin minifilament contains a number  $N_{\text{total}}$  of individual myosin heads and has a binding rate to the actin filament pair equal to

$$k_{\text{fil},\text{bind}} = N_{\text{total}} k_{\text{head},\text{bind}}, \quad (19)$$

where  $k_{\text{head},\text{bind}}$  is the individual myosin head binding rate. In MEDYAN,  $N_{\text{total}}$  is uniformly randomly selected between a minimum and maximum number of heads each time a minifilament binds. The bound myosin minifilament has a number of bound heads  $N_{\text{bound}}^0$  under zero tension equal to the duty ratio  $\rho$  times the total number of heads:

$$N_{\text{bound}}^0 = \rho N_{\text{total}}. \quad (20)$$

The duty ratio is determined by the individual head unbinding rate:

$$\rho = \frac{k_{\text{head},\text{bind}}}{k_{\text{head},\text{unbind}}^0 + k_{\text{head},\text{bind}}}, \quad (21)$$

where  $k_{\text{head},\text{unbind}}^0$  is the head unbinding rate under zero tension. Under tension  $F_{\text{ext}}$  the bound myosin minifilament has altered walking and unbinding rates as well as an altered number of bound heads. The number of bound heads under tension is given by

$$N_{\text{bound}}(F_{\text{ext}}) = \min \left\{ N_{\text{total}}, N_{\text{bound}}^0 + \beta \frac{F_{\text{ext}}}{N_{\text{total}}} \right\}, \quad (22)$$

where the parameter  $\beta = 2.0$  is chosen to fit experimental data. The myosin minifilament walking rate under zero tension is

$$k_{\text{fil},\text{walk}}^0 = s \frac{1 - \rho}{\rho} k_{\text{head},\text{bind}}, \quad (23)$$

where  $s$  is called the stepping fraction, defined as the ratio of the user-specified real distance between binding sites on the filament  $d_{\text{step}}$  to the distance between binding sites on the computational cylinder representing the filament segment  $d_{\text{total}}$ :  $s = \frac{d_{\text{step}}}{d_{\text{total}}}$ . Equation 23 is based on the PCM and is explained Refs. [18, 56]. Under tension, the myosin minifilament walking rate is altered according to a formula of the Hill type:

$$k_{\text{fil},\text{walk}} = \max \left\{ 0.0, k_{\text{fil},\text{walk}}^0 \frac{F_{\text{stall}} - F_{\text{ext}}}{F_{\text{stall}} + F_{\text{ext}}/\alpha} \right\}, \quad (24)$$

where the stall force  $F_{\text{stall}}$  is the maximum tension a minifilament can sustain before it stops walking, and where  $\alpha = 0.2$  is another parameter chosen to fit to experimental data. The myosin minifilament will unbind from the pair of actin filaments under zero tension with a rate

$$k_{\text{fil},\text{unbind}}^0 = \frac{k_{\text{head},\text{bind}} N_{\text{total}}}{\exp \left( \log \left( \frac{k_{\text{head},\text{unbind}}^0 + k_{\text{head},\text{bind}}}{k_{\text{head},\text{unbind}}^0} \right) N_{\text{total}} \right) - 1}. \quad (25)$$

This non-obvious expression is the inverse of the mean residence time of the minifilament as determined using the PCM. Under tension, the myosin minifilament unbinding is modeled with Kramers-type catch-bond behavior:

$$k_{\text{fil},\text{unbind}}(F_{\text{ext}}) = k_{\text{fil},\text{unbind}}^0 \max \left\{ 0.1, \exp \left( \frac{-F_{\text{ext}}}{N_{\text{bound}}(F_{\text{ext}}) F_{0,\text{head}}} \right) \right\}, \quad (26)$$

where  $F_{0,\text{head}}$  is the characteristic force a single myosin head catch-bond, and the minimum unbinding factor 0.1 is a parameter to chosen to ensure the possibility to unbind under arbitrarily large tension. We assume for myosin minifilaments that the stretching constant is given by

$$K_{\text{bound,str}} = K_{\text{head,str}} N_{\text{bound}}, \quad (27)$$

where  $K_{\text{head,str}}$  is the stretching constant for an individual head; this equation assumes the bound heads share the load in parallel.

The unbinding of passive cross-linkers (e.g.  $\alpha$ -actinin) are modeled are Kramers-type slip-bond:

$$k_{\text{linker,unbind}}(F_{\text{ext}}) = k_{\text{linker,unbind}}^0 \exp\left(-\frac{F_{\text{ext}}}{F_{0,\text{linker}}}\right), \quad (28)$$

where  $F_{0,\text{linker}}$  is the characteristic force of the cross-linker slip-bond.

Finally, the actin filament will polymerize with a rate that exponentially decreases with the component of the sustained force along the polymerizing tip,  $F_{\text{ext}}$ . This dependence is based on the Brownian ratchet model of Peskin et al. [76]:

$$k_{\text{poly}}(F_{\text{ext}}) = k_{\text{poly}}^0 \exp\left(-\frac{F_{\text{ext}}}{F_{0,\text{poly}}}\right), \quad (29)$$

where  $F_{0,\text{poly}}$  is the characteristic force of the Brownian ratchet model, and  $k_{\text{poly}}^0$  is the zero-force polymerization rate.

Any of the above characteristic forces  $F_0$  may be converted to a corresponding characteristic distance  $x_0$  via

$$F_0 = k_B T / x_0, \quad (30)$$

where  $k_B T$  is the thermal energy, casting expressions of the form  $F_{\text{ext}}/F_0$  to the form  $F_{\text{ext}}x_0/k_B T$ .

### A. Parameterization

The following table lists the parameters chosen for the simulations presented in this paper.

Parameter	Description	Value
<b>General Simulation Parameters</b>		
$k_B T$	Thermal energy	$4.1 \text{ pN} \cdot \text{nm}$
$L_{\text{comp}}$	Cubic compartment side length	$500 \text{ nm}$
$N_x, N_y, N_z$	Number of compartments in each dimension	2, 2, 2
$L_{\text{cyl}}$	Filament cylinder equilibrium length	$54 \text{ nm}$
$\delta t$	Length of chemical evolution step	$0.05 \text{ s}$
$F_T$	Force tolerance of mechanical minimization	$1 \text{ pN}$
<b>Mechanical Parameters</b>		
$K_{\text{fil,str}}$	Actin filament stretching constant	$100 \text{ pN/nm}$ [18]
$\epsilon_{\text{bend}}$	Actin filament bending energy	$1344 \text{ pN} \cdot \text{nm}$ [18, 77]
$K_{\text{vol}}$	Cylinder excluded volume constant	$10^5 \text{ pN/nm}^4$ [18]
$K_{\text{head,str}}$	NMIIA head stretching constant	$2.5 \text{ pN/nm}$ [78]
$K_{\alpha,\text{str}}$	$\alpha$ -actinin stretching constant	$8 \text{ pN/nm}$ [79]
$\epsilon_{\text{boundary}}$	Boundary repulsion energy	$41 \text{ pN} \cdot \text{nm}$ <sup>a</sup>
$\lambda$	Boundary repulsion screening length	$2.7 \text{ nm}$ <sup>b</sup>
<b>Mechanochemical Parameters</b>		
$N_{\text{NMIIA,bind}}$	Binding sites per cylinder for myosin motors	8 <sup>c</sup>
$N_{\alpha,\text{bind}}$	Binding sites per cylinder for $\alpha$ -actinin	4 <sup>d</sup>
$d_{\text{step}}$	NMIIA minifilament step size	$6.0 \text{ nm}$ [78]
$N_{\text{min}}, N_{\text{max}}$	Range of number of NMIIA heads per minifilament	15, 25 <sup>e</sup> [80]
$F_{\text{stall}}$	Stall force of NMIIA minifilament	$100 \text{ pN}$ <sup>f</sup>
$F_{0,\text{head}}$	Characteristic force of NMIIA catch-bond	$12.6 \text{ pN}$ [56]
$F_{0,\alpha}$	Characteristic force of $\alpha$ -actinin slip-bond	$17.2 \text{ pN}$ [81]
$F_{0,\text{poly}}$	Characteristic force of actin Brownian ratchet	$1.5 \text{ pN}$ [82]
$l_M$	Equilibrium length of NMIIA minifilament	$175 - 225 \text{ nm}$ [18]
$l_\alpha$	Equilibrium length of $\alpha$ -actinin	$30 - 40 \text{ nm}$ [18]
<b>Chemical Parameters</b>		
$k_{\text{actin,diff}}$	Diffusion constant of actin monomer	$20 \mu\text{M s}^{-1}$ [18]
$k_{\alpha,\text{diff}}$	Diffusion constant of $\alpha$ -actinin	$2 \mu\text{M s}^{-1}$ [18, 83]
$k_{\text{motor,diff}}$	Diffusion constant of NMIIA minifilament	$0.2 \mu\text{M s}^{-1}$ [18]
$k_{\text{actin,poly,+}}$	Actin plus-end polymerization	$11.6 \mu\text{M s}^{-1}$ [71]
$k_{\text{actin,poly,-}}$	Actin minus-end polymerization	$1.3 \mu\text{M s}^{-1}$ [71]
$k_{\text{actin,depoly,+}}$	Actin plus-end depolymerization	$1.4 \text{ s}^{-1}$ [71]
$k_{\text{actin,depoly,-}}$	Actin minus-end depolymerization	$0.8 \text{ s}^{-1}$ [71]
$k_{\text{head,bind}}$	NMIIA head binding	$0.2 \text{ s}^{-1}$ [55]
$k_{\text{head,unbind}}^0$	NMIIA head unbinding under zero tension	$1.7 \text{ s}^{-1}$ [18, 55]
$k_{\alpha,\text{bind}}$	$\alpha$ -actinin binding	$0.7 \mu\text{M s}^{-1}$ [84]
$k_{\alpha,\text{unbind}}^0$	$\alpha$ -actinin unbinding under zero tension	$0.3 \text{ s}^{-1}$ [84]

TABLE I. All parameters used in the simulations reported in this paper.

<sup>a</sup> - Chosen for the energy scale to be  $10 k_B T$ .

<sup>b</sup> - Chosen as the length of a G-actin monomer.

<sup>c</sup> - Chosen to allow the spacing between binding sites to be roughly equal to its physiological value near  $6 \text{ nm}$  [78].

<sup>d</sup> - Chosen to allow the spacing between binding sites to be roughly equal to its physiological value near  $30 \text{ nm}$  [85].

<sup>e</sup> - Chosen to given an average  $N_{\text{total}} = 20$  in approximate agreement with literature values [80].

<sup>f</sup> - A wide range of values are found in the literature for the stall force of the minifilament. We take an order of magnitude estimate for this parameter based on the stall force of a single head (on the order of  $10 \text{ pN}$ , estimated as  $d_{\text{step}} K_{\text{head,str}}$  [18]) times the number of bound heads in the minifilament (on the order of 10). This parameter choice is empirically valid as it yields observable network contraction.

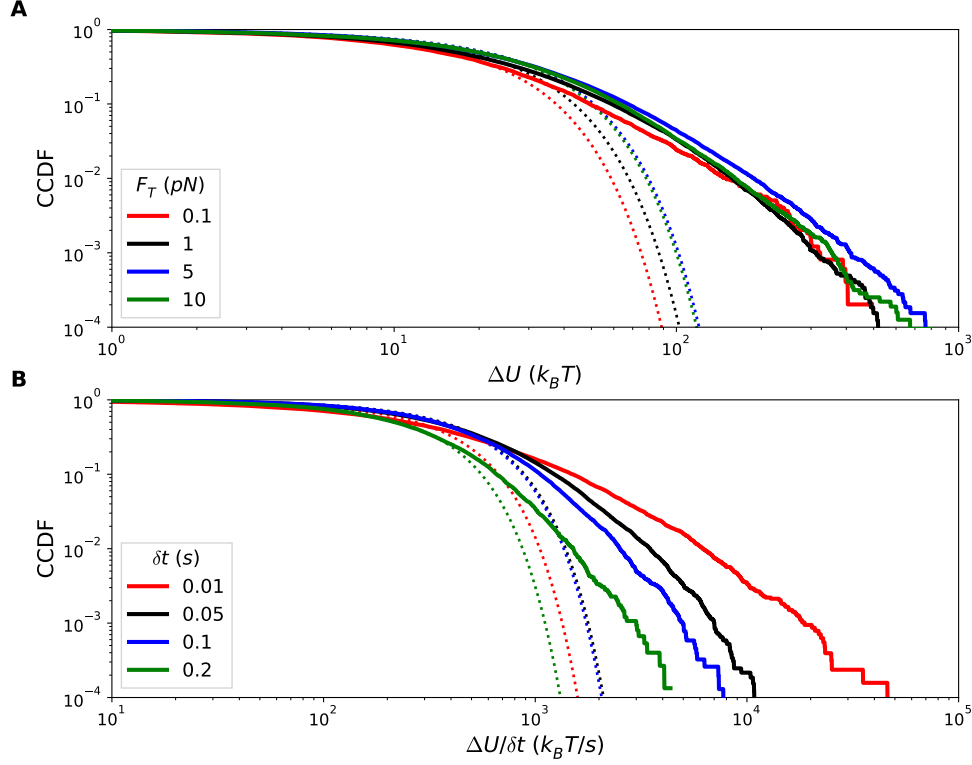


FIG. 10. **A:** Complementary cumulative distribution functions of the negative increments  $|\Delta U_-|$  at QSS for various choices of the force tolerance parameter  $F_T$  plotted against fitted half-normal CCDFs. For these runs condition  $C_{3,3}$  is used with  $\delta t = 0.05$  s. **B:** Complementary cumulative distribution functions of the negative increments  $|\Delta U_-|$  at QSS for various choices of the time between minimization,  $\delta t$ . The energy increments are normalized by  $\delta t$  for more direct comparison between these curves. For these runs condition  $C_{3,3}$  is used with  $F_T = 2$  pN.

### Dependence on $\delta t$ and $F_T$

The heavy-tailed distributions of  $|\Delta U_-|$ , the magnitudes of the negative energy increments which are the chief subject of this paper, may have strong dependence on certain key parameters governing the mechanical equilibration protocol. To ensure that these distributions are not artifacts of simulation we investigate whether changing the parameters  $F_T$  and  $\delta t$  alters the qualitative properties of the distributions. In Figure 10 we compare these distributions using 3 runs for each parameter choice. Only weak dependence on  $F_T$  is observed. We find strong dependence on  $\delta t$ , however for each parameter choice heavy tails exist and thus we may conclude that the cytoquake phenomenon is not an artifact despite their frequency and magnitude having dependence on  $\delta t$ . While a smaller choice for  $F_T$  and  $\delta t$  should correspond more closely to reality, we find that for the smallest of the tested values for these parameters the simulations did not complete in the allotted computer wall time of 2 weeks. Thus our choices for these parameters used in this paper are chosen to be small while still allowing us to run full 2,000 s simulations.

We also investigated how the fraction of negative eigenvalues persisting after mechanical minimization depends on the force threshold  $F_T$ . When minimization ceases at higher forces, more negative eigenvalues are left remaining, as expected. This behavior is illustrated in Figure 11.

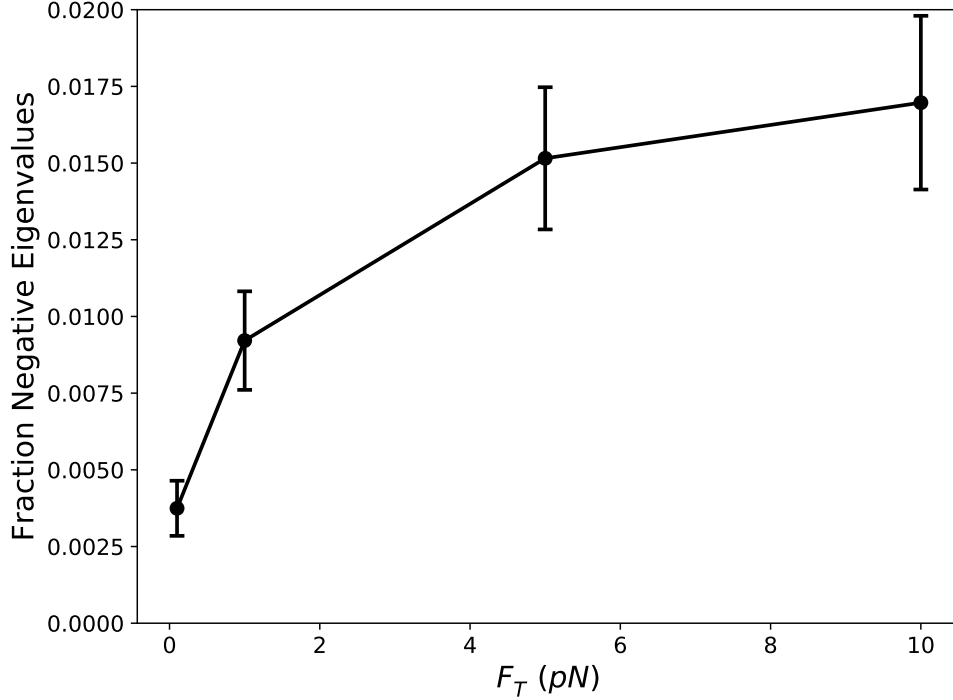


FIG. 11. Scatter plot showing the fraction of negative eigenvalues remaining after mechanical minimization when different choices of the parameter  $F_T$  are used. The data is collected from QSS for 3 runs of  $C_{3,3}$ , with the standard deviation taken over time and over the runs.

### Computing Filament Displacements

The area between the two filaments  $\mathbf{x}$  and  $\mathbf{y}$  is triangulated using the beads comprising the filaments ( $\{\mathbf{x}_i\}_{i=0}^{n_{\mathbf{x}}-1}$  and  $\{\mathbf{y}_j\}_{j=0}^{n_{\mathbf{y}}-1}$ ) as vertices, where  $n_{\mathbf{x}}$  is the number of beads in  $\mathbf{x}$  and similarly for  $n_{\mathbf{y}}$ . To compute the displacement of filament  $\mathbf{x}$  during the time interval  $\delta t$ , we set  $\mathbf{y}$  to the new configuration of  $\mathbf{x}$  at the end of the interval. The triangles come in pairs for most of the filament lengths, as shown using the dark and light colors of green of Figure 12. If  $n_{\mathbf{x}}$  and  $n_{\mathbf{y}}$  are unequal (say  $n_{\mathbf{x}} < n_{\mathbf{y}}$ ), extra triangles are added using the last bead in  $\mathbf{x}$ ,  $\mathbf{x}_{n_{\mathbf{x}}-1}$ , as the only vertex in filament  $\mathbf{x}$ . The sum of these triangle areas  $A_{\text{tot}}$  is divided by the average of the two filament contour lengths  $L_{\mathbf{x}}$  and  $L_{\mathbf{y}}$  to give the measure of distance  $d = \frac{2A_{\text{tot}}}{L_{\mathbf{x}} + L_{\mathbf{y}}}$ .

### Machine Learning Pipeline

#### 1. Cytoquake Classification

We pose the forecasting of cytoquakes as a binary classification problem. A trajectory  $\Delta U(t) = U(t + \delta t) - U(t)$  at QSS (after 1,000 s) is converted to a binary sequence such that each  $t$  for which  $\Delta U(t) \leq \Delta U_T$ , as well as the  $t_W = 0.15$  previous seconds (i.e. 3 previous time points) are classified as cytoquakes, and the rest are not. This  $t_W$  window is chosen to help overcome the stochasticity inherent in the chemical dynamics which, along with the instantaneous mechanical stability we are using as a predictor, controls cytoquake occurrence. We focus here on the 5 runs of conditions  $C_{3,3}$ .  $\Delta U_T = -100 k_B T$  is chosen to lie well in the tail of the distribution of  $|\Delta U_-|$  for this condition and therefore distinguishes rare events, as shown in Figure 2.B in the main text. With these choices,  $\sim 10\%$  of samples across all runs are labeled as events in the classification problem.

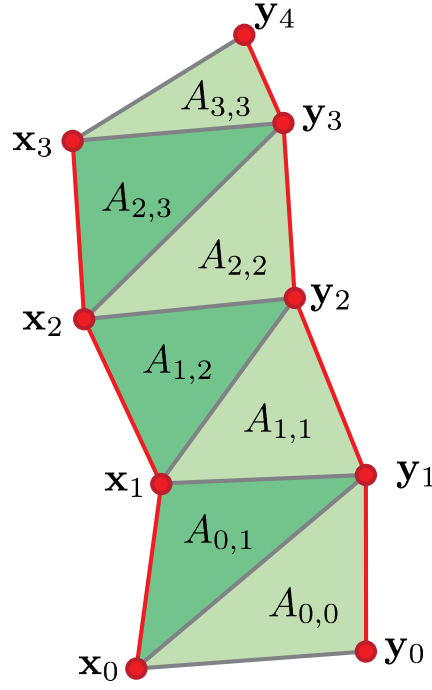


FIG. 12. Illustration of how the area between two filaments  $\mathbf{x}$  and  $\mathbf{y}$  is triangulated to allow calculation of the distance between them. The beads comprising the filaments are labeled  $\mathbf{x}_i$ ,  $\mathbf{y}_j$ , and areas between triplets of beads are labeled  $A_{i,j}$  where the lowest indices of the beads  $\mathbf{x}_i$  and  $\mathbf{y}_j$  in the triplet are used.

## 2. Model Inputs

The predictors of the model capture information about the network's mechanical stability. The ordered sets of eigenvalues  $\{\lambda_k\}_{k=1}^{3N}$  at each time  $t$  is padded by adding zero eigenvalues between the unstable ( $\lambda_k < 0$ ) and stable ( $\lambda_k \geq 0$ ) parts of the spectrum to maintain a fixed input dimension across all time points and runs. We then collect these eigenvalues into a vector  $\mathbf{M}(t)$  such that the first element of  $\mathbf{M}(t)$  is the largest negative  $\lambda_k$  at time  $t$  and the last element is the largest positive  $\lambda_k$  at time  $t$ . We optionally include the inverse participation ratios  $\{r_k\}_{k=1}^{3N}$  in this vector by first adding zeros in the places of the set  $\{r_k\}_{k=1}^{3N}$  corresponding to where zeros were added in the set  $\{\lambda_k\}_{k=1}^{3N}$ , and then interleaving the  $\lambda_k$  and  $r_k$  in the now doubly sized vector  $\mathbf{M}(t)$ , so that now for example the first two elements of  $\mathbf{M}(t)$  correspond to the largest negative  $\lambda_k$  and the associated  $r_k$  at time  $t$ . The vectors  $\mathbf{M}(t)$  are then linearly rescaled, so for each element  $M_i(t)$  the average over all times of a run is 0 and the variance is 1. These rescaled vectors are labeled  $\widetilde{\mathbf{M}}(t)$ .

When only the  $\lambda_k$  are included then  $\widetilde{\mathbf{M}}(t)$  has  $\sim 1,600$  dimensions, and with the  $r_k$  are also included it has  $\sim 3,200$  dimensions. To avoid overfitting the model, we first reduce the dimensionality of  $\widetilde{\mathbf{M}}(t)$  via PCA using all time points in a run. We choose 30 dimensions as the size of the reduced vector  $\mathbf{m}(t)$  because this allows for more than 95% of the variance of  $\widetilde{\mathbf{M}}(t)$  to be explained when just the  $\lambda_k$  are included as shown in Figure 4.A in the main text. Model performance appreciably decreases when fewer than 30 dimension are used and improves only marginally if more are used. A row of ones is added as a 31<sup>st</sup> dimension to  $\mathbf{m}(t)$  as a bias for the neural network. As an additional indicator of the network's mechanical stability we may also consider its mechanical energy at time  $t$ . The original mechanical energy  $U(t)$  is linearly rescaled to give  $\widetilde{U}(t)$  so that it has zero mean and unit variance. We then optionally augment with input vector  $\mathbf{m}(t)$  with the  $\widetilde{U}(t)$  as a 32<sup>nd</sup> dimension.



### 3. Treating Multiple Trials

We may treat the data from all 5 runs of condition  $C_{3,3}$  separately or combine all data together to train a larger model. Model performance is generally found to be better when trained on data from a single run, however by combining data from all runs we probe more general underlying trends that are not specific to the network organization of one run. When describing trends from varying model inputs as in Figure 4.D in the main text, we focus on results obtained by combining all runs due to their greater generality.

For a single run there are  $\sim 20,000$  samples, giving 100,000 samples when combining all runs. When combining runs, we first rescale and perform PCA on the predictors using only the data within a single run, and then concatenate the resulting  $\mathbf{m}(t)$  with their associated labels into a larger data set. This way the relative variation of the predictors compared to their typical values for a particular organization of the actomyosin network is retained, and the typical values of particular network organizations themselves affect the model inputs to a lesser degree.

### 4. Neural Network Architecture

We used the Python modules scikit-learn and Keras with a Tensorflow back end to train a deep feed-forward neural network and a logistic regression model for the binary classification problem [86, 87]. The 31 or 32-dimensional (depending on if  $\tilde{U}(t)$  is included as a predictor) input vector  $\mathbf{m}$  is fed into three fully connected hidden layers  $L_i$ ,  $i = 1, 2, 3$ , each with either 30 or 100 nodes depending on if the data consists of a single run (20,000 samples) or of all 5 runs (100,000 samples). Each node in the hidden layers uses a rectified linear unit activation function. The output of the network is two nodes using a softmax activation function whose values are  $p$  and  $1 - p$ , where  $p$  is the predicted probability of a cytoquake event at that time  $t$ . The network is trained for either 400 or 200 epochs using a categorical cross-entropy loss function with Adam optimization in stochastically chosen batches of either 1,000 or 10,000 samples, depending on the whether the single or multiple run data sets, respectively, are used. The cytoquake samples are given a higher weight ( $\times 3$ ) than the non-cytoquake samples during training. A L2 penalty of 0.05 is used to curb overfitting. When using only  $\tilde{U}(t)$  as a predictor, a logistic regression model is fit using the same sample weights.

### 5. Model Validation

Of all the data samples, we use 2/3 to train the model with and validate the model on the remaining 1/3. We repeat these random training/testing set splits to gather statistics on model performance. The binary classification procedure involves the probability threshold  $p_T$  (such that  $p > p_T$  means the model predicts a cytoquake). Model performance is measured by varying  $p_T$  from 0 to 1 and measuring the true positive rate (TPR, the proportion of actual cytoquakes correctly predicted as such) and false positive rate (FPR, the proportion of actual non-cytoquakes incorrectly predicted as cytoquakes) on the test data; the locus of these points forms the receiver operator characteristic (ROC) curve. A random model would have  $\text{FPR} = \text{TPR}$ , so an area under the curve (AUC) of the ROC curve greater than 0.5 indicates a good model, and a perfect model would have an AUC of 1. One can also consider precision-recall (PR) curves, which contain points in the space of model precision (the proportion of predicted cytoquakes which were actual cytoquakes) and recall (the same as TPR). A random model would have the same precision, equal to the proportion of actual cytoquakes in the testing data, for all values of recall as  $p_T$  is varied, giving an AUC equal to that proportion.

When the test data is unbalanced, i.e. when there are many more non-cytoquake events than cytoquake events, it has been shown that the AUC of the PR curve is a more faithful metric for model performance (since a model may score a high AUC of the ROC curve by overestimating that events are not cytoquakes) [68, 69]. To overcome this limitation of ROC curves, which we believe has a more intuitive interpretation than PR curves, we balance the testing data, keeping all cytoquake events and randomly keeping an equal number of non-cytoquake events. We confirmed that trends observed in the AUC of the ROC curves as the model is varied also hold when considering the AUC of PR curves on the full test set.

In Figure 13 we show examples of these PR and ROC curves on the training and testing data for a model trained on a single run. The very high AUC of the PR and ROC curves evaluated on the training data

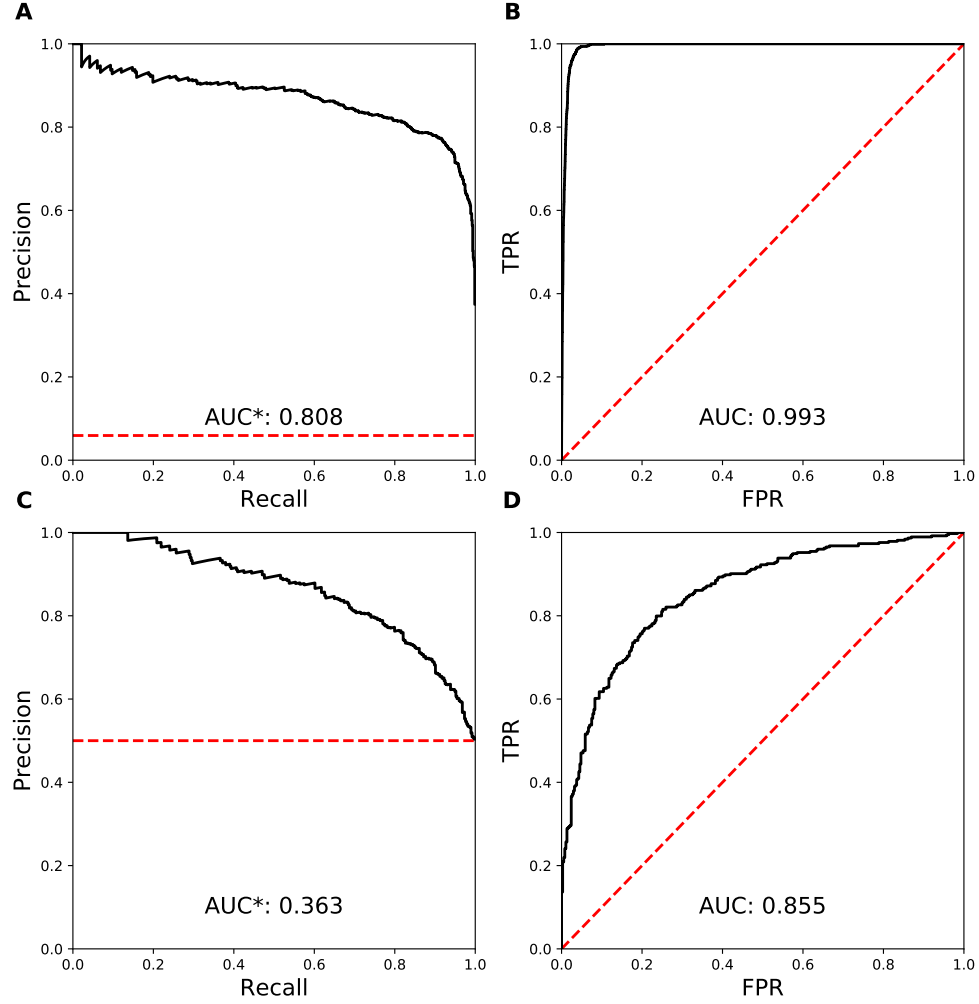


FIG. 13. **A:** PR curve evaluated for a model using  $\{\lambda_k\}_{k=1}^{3N}$ ,  $\{r_k\}_{k=1}^{3N}$ , and  $U$  as inputs trained on data from a single run at QSS of condition  $C_{3,3}$  and evaluated on the training data. The red line indicates the performance of a random model on the data set. The asterisk on the AUC indicates that the fraction of cytoquake samples in the data set (for this run  $\sim 0.06$ ) has been subtracted from the actual AUC, to give the area between the black and red curves. **B:** ROC curve for the same model evaluated on the training data. **C:** PR curve for the same model evaluated on the balanced testing data. **D:** ROC curve for the same model evaluated on the balanced testing data.

indicates that the model has nearly perfected its prediction on those samples and may indicate overfitting, however this high performance generalizes nicely to the unseen testing data. Note that the AUC of the ROC evaluated on the testing data is significantly higher than shown in Figure 4.D in the main text reflecting the generally higher performance of models trained on data from a single run compared to models trained on data from all runs.

Finally, as a sanity check, we confirmed that randomly shuffling the labels on the training set decreases performance on the training set and causes the performance on the test set to decrease to that of a random model, as shown in Figure 14.

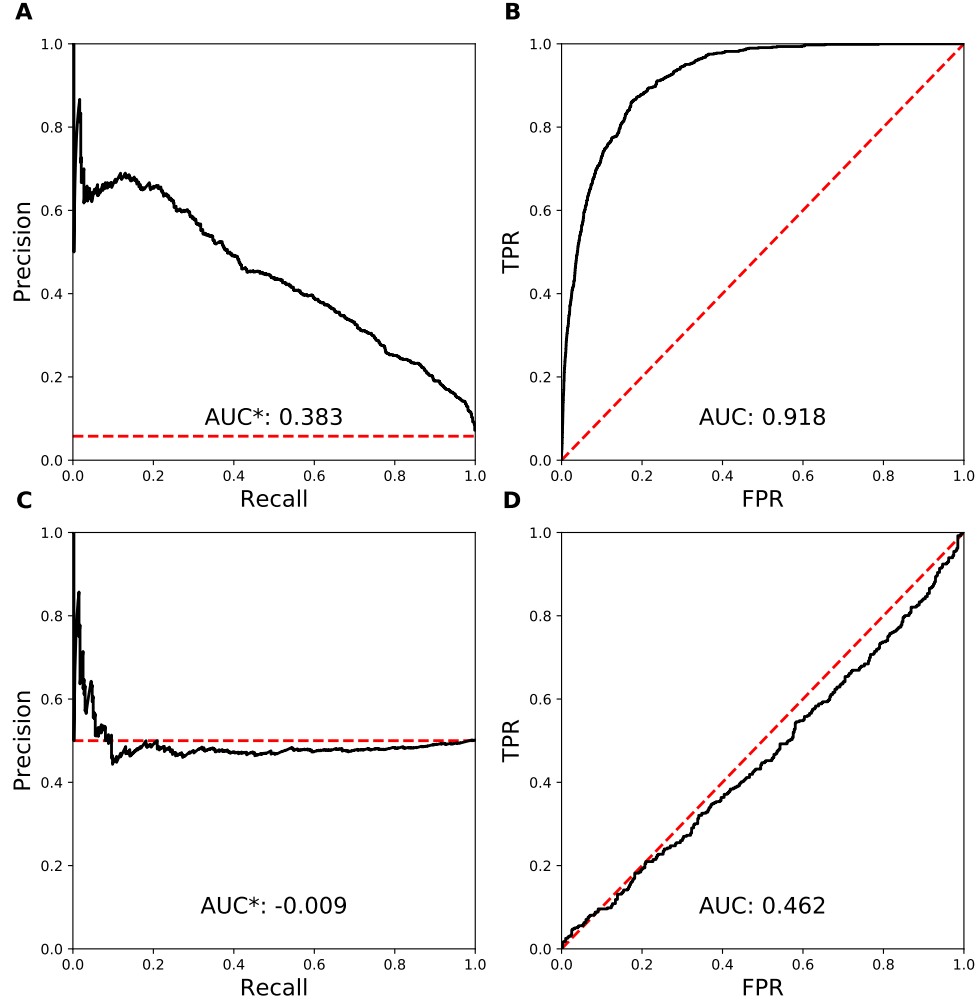


FIG. 14. **A:** PR curve evaluated for a model using  $\{\lambda_k\}_{k=1}^{3N}$ ,  $\{r_k\}_{k=1}^{3N}$ , and  $U$  as inputs trained on data from a single run at QSS of condition  $C_{3,3}$  and evaluated on the training data, when the training data labels have been randomly shuffled. The red line indicates the performance of a random model on the data set. **B:** ROC curve for the same model evaluated on the training data. **C:** PR curve for the same model evaluated on the balanced testing data. **D:** ROC curve for the same model evaluated on the balanced testing data.

- 
- [1] Daniel A Fletcher and R Dyche Mullins. Cell mechanics and the cytoskeleton. *Nature*, 463(7280):485–492, 2010.
  - [2] David Boal. *Mechanics of the Cell*. Cambridge University Press, 2012.
  - [3] R Tyler McLaughlin et al. Collective dynamics of processive cytoskeletal motors. *Soft matter*, 12(1):14–21, 2016.
  - [4] Toshihiro Toyota, David A Head, Christoph F Schmidt, and Daisuke Mizuno. Non-gaussian athermal fluctuations in active gels. *Soft Matter*, 7(7):3234–3239, 2011.
  - [5] Fred C MacKintosh and Alex J Levine. Nonequilibrium mechanics and dynamics of motor-activated gels. *Physical review letters*, 100(1):018104, 2008.
  - [6] Adriano Mesquita Alencar, Mariana Sacchini Ayres Ferraz, Chan Young Park, Emil Millet, Xavier Trepas, Jeffrey J Fredberg, and James P Butler. Non-equilibrium cytoquake dynamics in cytoskeletal remodeling and stabilization. *Soft matter*, 12(41):8506–8511, 2016.
  - [7] Yu Shi, Christopher L Porter, John C Crocker, and Daniel H Reich. Dissecting fat-tailed fluctuations in the cytoskeleton with active micropost arrays. *Proceedings of the National Academy of Sciences*, 116(28):13839–13846, 2019.
  - [8] Carlos Floyd, Garegin A Papoian, and Christopher Jarzynski. Quantifying dissipation in actomyosin networks. *Interface focus*, 9(3):20180078, 2019.
  - [9] Beno Gutenberg and Charles Richter. *Seismicity of the earth and associated phenomena*. Princeton University Press, 1949.
  - [10] Per Bak, Kim Christensen, Leon Danon, and Tim Scanlon. Unified scaling law for earthquakes. *Physical Review Letters*, 88(17):178501, 2002.
  - [11] Martin van Hecke. Jamming of soft particles: geometry, mechanics, scaling and isostaticity. *Journal of Physics: Condensed Matter*, 22(3):033101, 2009.
  - [12] Jean-Philippe Bouchaud. Weak ergodicity breaking and aging in disordered systems. *Journal de Physique I*, 2(9):1705–1713, 1992.
  - [13] Laetitia Kurzawa, Benoit Vianay, Fabrice Senger, Timothée Vignaud, Laurent Blanchoin, and Manuel Théry. Dissipation of contractile forces: the missing piece in cell mechanics. *Molecular biology of the cell*, 28(14):1825–1832, 2017.
  - [14] Christopher Langton. Computation at the edge of chaos: Phase transition and emergent computation. Technical report, Los Alamos National Lab., NM (USA), 1990.
  - [15] Tim Mitchison and Marc Kirschner. Dynamic instability of microtubule growth. *nature*, 312(5991):237–242, 1984.
  - [16] Pavel I Zhuravlev and Garegin A Papoian. Molecular noise of capping protein binding induces macroscopic instability in filopodial dynamics. *Proceedings of the National Academy of Sciences*, 106(28):11570–11575, 2009.
  - [17] James J Binney, Nigel J Dowrick, Andrew J Fisher, and Mark EJ Newman. *The theory of critical phenomena: an introduction to the renormalization group*. Oxford University Press, 1992.
  - [18] Konstantin Popov, James Komianos, and Garegin A Papoian. Medyan: mechanochemical simulations of contraction and polarity alignment in actomyosin networks. *PLoS computational biology*, 12(4), 2016.
  - [19] Aravind Chandrasekaran, Arpita Upadhyaya, and Garegin A Papoian. Remarkable structural transformations of actin bundles are driven by their initial polarity, motor activity, crosslinking, and filament treadmilling. *PLoS computational biology*, 15(7), 2019.
  - [20] Qin Ni and Garegin A Papoian. Turnover versus treadmilling in actin network assembly and remodeling. *Cytoskeleton*, 2019.
  - [21] Xiaona Li, Qin Ni, Xiuxiu He, Jun Kong, Soon-Mi Lim, Garegin A Papoian, Jerome P Trzeciakowski, Andreea Trache, and Yi Jiang. Tensile force induced cytoskeletal reorganization: Mechanics before chemistry. *BioRxiv*, 2020.
  - [22] Carlos Floyd, Garegin A Papoian, and Christopher Jarzynski. Gibbs free energy change of a discrete chemical reaction event. *The Journal of Chemical Physics*, 152(8):084116, 2020.
  - [23] James E Komianos and Garegin A Papoian. Stochastic ratcheting on a funneled energy landscape is necessary for highly efficient contractility of actomyosin force dipoles. *Physical Review X*, 8(2):021006, 2018.
  - [24] Shenshen Wang and Peter G Wolynes. Active contractility in actomyosin networks. *Proceedings of the National Academy of Sciences*, 109(17):6446–6451, 2012.
  - [25] Bruce D Malamud and Donald L Turcotte. Self-affine time series: I. generation and analyses. *Adv. Geophys.*, 40:1–90, 1999.
  - [26] Jon D Pelletier and Donald L Turcotte. Self-affine time series: II. applications and models. In *Advances in Geophysics*, volume 40, pages 91–166. Elsevier, 1999.
  - [27] Donald L Turcotte. *Fractals and chaos in geology and geophysics*. Cambridge university press, 1997.
  - [28] Stefan Hergarten. *Self organized criticality in earth systems*, volume 2. Springer, 2002.
  - [29] Annette Witt and Bruce D Malamud. Quantification of long-range persistence in geophysical time series: conventional and benchmark-based improvement techniques. *Surveys in Geophysics*, 34(5):541–651, 2013.
  - [30] ZC Williams, JD Pelletier, and Thomas Meixner. Self-affine fractal spatial and temporal variability of the san

- pedro river, southern arizona. *Journal of Geophysical Research: Earth Surface*, 124(6):1540–1558, 2019.
- [31] Ian Linsmeier, Shiladitya Banerjee, Patrick W Oakes, Wonyeong Jung, Taeyoon Kim, and Michael P Murrell. Disordered actomyosin networks are sufficient to produce cooperative and telescopic contractility. *Nature communications*, 7(1):1–9, 2016.
  - [32] Henrik Jeldtoft Jensen. *Self-organized criticality: emergent complex behavior in physical and biological systems*, volume 10. Cambridge university press, 1998.
  - [33] Daniel S Seara, Vikrant Yadav, Ian Linsmeier, A Pasha Tabatabai, Patrick W Oakes, SM Ali Tabei, Shiladitya Banerjee, and Michael P Murrell. Entropy production rate is maximized in non-contractile actomyosin. *Nature communications*, 9(1):1–10, 2018.
  - [34] Chon-Kit Pun, Sakib Matin, W Klein, and Harvey Gould. Prediction in a driven-dissipative system displaying a continuous phase transition using machine learning. *Physical Review E*, 101(2):022102, 2020.
  - [35] Tamar Schlick. *Molecular modeling and simulation: an interdisciplinary guide: an interdisciplinary guide*, volume 21. Springer Science & Business Media, 2010.
  - [36] Andrew R Leach and Andrew R Leach. *Molecular modelling: principles and applications*. Pearson education, 2001.
  - [37] Minhaeng Cho, Graham R Fleming, Shinji Saito, Iwao Ohmine, and Richard M Stratt. Instantaneous normal mode analysis of liquid water. *The Journal of chemical physics*, 100(9):6672–6683, 1994.
  - [38] Scott D Bembenek and Brian B Laird. Instantaneous normal modes and the glass transition. *Physical review letters*, 74(6):936, 1995.
  - [39] Kurt Broderix, Kamal K Bhattacharya, Andrea Cavagna, Annette Zippelius, and Irene Giardina. Energy landscape of a lennard-jones liquid: Statistics of stationary points. *Physical review letters*, 85(25):5360, 2000.
  - [40] Phoebe MR DeVries, Fernanda Viégas, Martin Wattenberg, and Brendan J Meade. Deep learning of aftershock patterns following large earthquakes. *Nature*, 560(7720):632–634, 2018.
  - [41] Arnaud Mignan and Marco Broccardo. One neuron versus deep learning in aftershock prediction. *Nature*, 574(7776):E1–E3, 2019.
  - [42] Leonardo E Silbert, Andrea J Liu, and Sidney R Nagel. Normal modes in model jammed systems in three dimensions. *Physical Review E*, 79(2):021308, 2009.
  - [43] Zorana Zeravcic, Wim van Saarloos, and David R Nelson. Localization behavior of vibrational modes in granular packings. *EPL (Europhysics Letters)*, 83(4):44001, 2008.
  - [44] Tongye Shen and Peter G Wolynes. Stability and dynamics of crystals and glasses of motorized particles. *Proceedings of the National Academy of Sciences*, 101(23):8547–8550, 2004.
  - [45] Shenshen Wang and Peter G Wolynes. Communication: Effective temperature and glassy dynamics of active matter, 2011.
  - [46] Shenshen Wang and Peter G Wolynes. Microscopic theory of the glassy dynamics of passive and active network materials. *The Journal of chemical physics*, 138(12):12A521, 2013.
  - [47] G Ouillon, C Castaing, and D Sornette. Hierarchical geometry of faulting. *Journal of Geophysical Research: Solid Earth*, 101(B3):5477–5487, 1996.
  - [48] Sanaz Sadegh, Jenny L Higgins, Patrick C Mannion, Michael M Tamkun, and Diego Krapf. Plasma membrane is compartmentalized by a self-similar cortical actin meshwork. *Physical Review X*, 7(1):011031, 2017.
  - [49] SF Tebbens, SM Burroughs, Christopher C Barton, and DF Naar. Statistical self-similarity of hotspot seamount volumes modeled as self-similar criticality. *Geophysical research letters*, 28(14):2711–2714, 2001.
  - [50] Sarah F Tebbens and Stephen M Burroughs. Forest fire burn areas in western canada modeled as self-similar criticality. *Physica D: Nonlinear Phenomena*, 211(3-4):221–234, 2005.
  - [51] Ch H Scholz and CA Aviles. The fractal geometry of faults and faulting. *Earthquake source mechanics*, 37:147–155, 1986.
  - [52] Hiroo Kanamori and Don L Anderson. Theoretical basis of some empirical relations in seismology. *Bulletin of the seismological society of America*, 65(5):1073–1095, 1975.
  - [53] Randall Marrett and Richard W Allmendinger. Estimates of strain due to brittle faulting: sampling of fault populations. *Journal of Structural Geology*, 13(6):735–738, 1991.
  - [54] Carlos Floyd, Christopher Jarzynski, and Garegin Papoian. Low-dimensional manifold of actin polymerization dynamics. *New Journal of Physics*, 19(12):125012, 2017.
  - [55] Mihály Kovács, Fei Wang, Aihua Hu, Yue Zhang, and James R Sellers. Functional divergence of human cytoplasmic myosin ii kinetic characterization of the non-muscle iia isoform. *Journal of Biological Chemistry*, 278(40):38132–38140, 2003.
  - [56] Thorsten Erdmann, Philipp J Albert, and Ulrich S Schwarz. Stochastic dynamics of small ensembles of non-processive molecular motors: The parallel cluster model. *The Journal of chemical physics*, 139(17):11B604-1, 2013.
  - [57] Jonathon Howard et al. Mechanics of motor proteins and the cytoskeleton. 2001.
  - [58] Carol A Otey and Olli Carpen.  $\alpha$ -actinin revisited: A fresh look at an old player. *Cell motility and the cytoskeleton*, 58(2):104–111, 2004.
  - [59] O Lieleg, Mireille Maria Anna Elisabeth Claessens, Y Luan, and AR Bausch. Transient binding and dissipation

- in cross-linked actin networks. *Physical review letters*, 101(10):108101, 2008.
- [60] James Liman, Carlos Bueno, Yossi Eliaz, Nicholas P Schafer, M Neal Waxham, Peter G Wolynes, Herbert Levine, and Margaret S Cheung. The role of the arp2/3 complex in shaping the dynamics and structures of branched actomyosin networks. *Proceedings of the National Academy of Sciences*, 2020.
  - [61] David Keller and Carlos Bustamante. The mechanochemistry of molecular motors. *Biophysical journal*, 78(2):541–556, 2000.
  - [62] Yuriy V Pereverzev, Oleg V Prezhdo, Manu Forero, Evgeni V Sokurenko, and Wendy E Thomas. The two-pathway model for the catch-slip transition in biological adhesion. *Biophysical journal*, 89(3):1446–1454, 2005.
  - [63] Ron Milo and Rob Phillips. *Cell biology by the numbers*. Garland Science, 2015.
  - [64] Bernard R Brooks, Dušanka Janežič, and Martin Karplus. Harmonic analysis of large systems. i. methodology. *Journal of computational chemistry*, 16(12):1522–1542, 1995.
  - [65] Yann N Dauphin, Razvan Pascanu, Caglar Gulcehre, Kyunghyun Cho, Surya Ganguli, and Yoshua Bengio. Identifying and attacking the saddle point problem in high-dimensional non-convex optimization. In *Advances in neural information processing systems*, pages 2933–2941, 2014.
  - [66] Mark Newman. *Networks*. Oxford university press, 2018.
  - [67] José Alvarado, Michael Sheinman, Abhinav Sharma, Fred C MacKintosh, and Gijsje H Koenderink. Force percolation of contractile active gels. *Soft matter*, 13(34):5624–5644, 2017.
  - [68] Jesse Davis and Mark Goadrich. The relationship between precision-recall and roc curves. In *Proceedings of the 23rd international conference on Machine learning*, pages 233–240, 2006.
  - [69] Takaya Saito and Marc Rehmsmeier. The precision-recall plot is more informative than the roc plot when evaluating binary classifiers on imbalanced datasets. *PloS one*, 10(3), 2015.
  - [70] Tobias T Falzone, Savanna Blair, and Rae M Robertson-Anderson. Entangled f-actin displays a unique crossover to microscale nonlinearity dominated by entanglement segment dynamics. *Soft matter*, 11(22):4418–4423, 2015.
  - [71] Ikuko Fujiwara, Dimitrios Vavylonis, and Thomas D Pollard. Polymerization kinetics of adp-and adp-pi-actin determined by fluorescence microscopy. *Proceedings of the National Academy of Sciences*, 104(21):8827–8832, 2007.
  - [72] Olaf Wolkenhauer, Peter Wellstead, Kwang-Hyun Cho, Ramon Grima, and Santiago Schnell. Modelling reaction kinetics inside cells. *Essays in biochemistry*, 45:41–56, 2008.
  - [73] David Bernstein. Simulating mesoscopic reaction-diffusion systems using the gillespie algorithm. *Physical Review E*, 71(4):041103, 2005.
  - [74] Daniel T Gillespie. Exact stochastic simulation of coupled chemical reactions. *The journal of physical chemistry*, 81(25):2340–2361, 1977.
  - [75] Thorsten Erdmann, Kathrin Bartelheimer, and Ulrich S Schwarz. Sensitivity of small myosin ii ensembles from different isoforms to mechanical load and atp concentration. *Physical Review E*, 94(5):052403, 2016.
  - [76] Charles S Peskin, Garrett M Odell, and George F Oster. Cellular motions and thermal fluctuations: the brownian ratchet. *Biophysical journal*, 65(1):316–324, 1993.
  - [77] A Ott, M Magnasco, A Simon, and A Libchaber. Measurement of the persistence length of polymerized actin using fluorescence microscopy. *Physical Review E*, 48(3):R1642, 1993.
  - [78] Andrej Vilfan and Thomas Duke. Instabilities in the transient response of muscle. *Biophysical Journal*, 85(2):818–827, 2003.
  - [79] BA DiDonna and Alex J Levine. Unfolding cross-linkers as rheology regulators in f-actin networks. *Physical Review E*, 75(4):041909, 2007.
  - [80] Neil Billington, Aibing Wang, Jian Mao, Robert S Adelstein, and James R Sellers. Characterization of three full-length human nonmuscle myosin ii paralogs. *Journal of Biological Chemistry*, 288(46):33398–33410, 2013.
  - [81] Jorge M Ferrer, Hyungsuk Lee, Jiong Chen, Benjamin Pelz, Fumihiko Nakamura, Roger D Kamm, and Matthew J Lang. Measuring molecular rupture forces between single actin filaments and actin-binding proteins. *Proceedings of the National Academy of Sciences*, 105(27):9221–9226, 2008.
  - [82] Matthew J Footer, Jacob WJ Kerssemakers, Julie A Theriot, and Marileen Dogterom. Direct measurement of force generation by actin filament polymerization using an optical trap. *Proceedings of the National Academy of Sciences*, 104(7):2181–2186, 2007.
  - [83] Longhua Hu and Garegin A Papoian. Mechano-chemical feedbacks regulate actin mesh growth in lamellipodial protrusions. *Biophysical journal*, 98(8):1375–1384, 2010.
  - [84] Daniel H Wachsstock, WH Schwartz, and Thomas D Pollard. Affinity of alpha-actinin for actin determines the structure and mechanical properties of actin filament gels. *Biophysical journal*, 65(1):205, 1993.
  - [85] Rudolf K Meyer and Ueli Aebi. Bundling of actin filaments by alpha-actinin depends on its molecular length. *The Journal of cell biology*, 110(6):2013–2024, 1990.
  - [86] François Chollet et al. Keras. <https://keras.io>, 2015.
  - [87] F. Pedregosa, G. Varoquaux, A. Gramfort, V. Michel, B. Thirion, O. Grisel, M. Blondel, P. Prettenhofer, R. Weiss, V. Dubourg, J. Vanderplas, A. Passos, D. Cournapeau, M. Brucher, M. Perrot, and E. Duchesnay. Scikit-learn: Machine learning in Python. *Journal of Machine Learning Research*, 12:2825–2830, 2011.